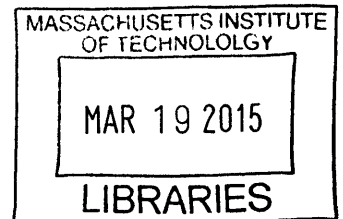


**Timing Performance of Superconducting Nanowire  
Single-Photon Detectors**

ARCHIVES

by  
Faraz Najafi



Submitted to the Department of Electrical Engineering and Computer  
Science

in partial fulfillment of the requirements for the degree of

Master of Science in Electrical Engineering

at the

MASSACHUSETTS INSTITUTE OF TECHNOLOGY

February 2015

© Massachusetts Institute of Technology 2015. All rights reserved.

**Signature redacted**

Author .....  
Department of Electrical Engineering and Computer Science  
January 28, 2015

**Signature redacted**

Certified by .....  
Karl K. Berggren  
Professor of Electrical Engineering and Computer Science  
Thesis Supervisor

**Signature redacted**

Accepted by .....  
Leslie A. Kolodziejski  
Professor of Electrical Engineering and Computer Science  
Chairman, Department Committee on Graduate Theses



# Timing Performance of Superconducting Nanowire Single-Photon Detectors

by

Faraz Najafi

Submitted to the Department of Electrical Engineering and Computer Science  
on January 28, 2015, in partial fulfillment of the  
requirements for the degree of  
Master of Science in Electrical Engineering

## Abstract

Superconducting nanowire single-photon detectors (SNSPDs) are becoming increasingly popular for applications in quantum information and long-distance communication. While the detection efficiency of SNSPDs has significantly improved over time, their timing performance has largely remained unchanged. Furthermore, the photodetection process in superconducting nanowires is still not fully understood and subject to ongoing research. In this thesis, I will present a systematic study of the timing performance of different types of nanowire single-photon detectors. I will analyze the photodetection delay histogram (also called instrument response function IRF) of these detectors as a function of bias current, nanowire width and wavelength. The study of the IRF yielded several unexpected results, among them a wavelength-dependent exponential tail of the IRF and a discrepancy between experimental photodetection delay results and the predicted value based on the electrothermal model. These results reveal some shortcomings of the basic models used for SNSPDs, and may include a signature of the initial process by which photons are detected in superconducting nanowires. I will conclude this thesis by presenting a brief introduction into vortices, which have recently become a popular starting point for photodetection models for SNSPDs. Building on prior work, I will show that a simple image method can be used to calculate the current flow in presence of a vortex, and discuss possible implications of recent vortex-based models for timing jitter.

Thesis Supervisor: Karl K. Berggren

Title: Professor of Electrical Engineering and Computer Science



# Acknowledgments

The work presented in this thesis was made possible by the advice, support and contributions of many people. I would like to thank:

Professor Karl K. Berggren for teaching me about nano-fabrication and SNSPDs, and his guidance, advice and support throughout grad school;

Dr. Francesco Marsili for teaching me a lot of experimental skills, and for fabricating some of the detectors and running some of the electrothermal simulations used for chapter 3 of this thesis;

Professor Terry Orlando for teaching me about superconductivity, and for his guidance during the compilation of chapter 5 of this thesis;

Dr. Eric Dauler and Dr. Vikas Anant for many helpful discussions, and for fabricating some of the detectors used for chapter 4 of this thesis;

Adam McCaughan and Quinyuan Zhao for help and support in the lab, and for performing some of the electrothermal simulations used for chapter 4 of this thesis;

Jim Daley and Mark Mondol for technical support in the lab;

And finally many past and present members of the Quantum Nanostructures and Nanofabrication Group not mentioned here who have helped me along the way.

I would also like to thank the Center for Excitonics (Award No. DE- SC0001088) for funding the presented work in 2010/2011 and the DARPA InPho program (Award

No. W911NF-10-1-0416) for funding the work in 2011/2012.

# Contents

<b>1</b>	<b>Introduction</b>	<b>19</b>
1.1	Single-photon detectors . . . . .	19
1.1.1	Classification . . . . .	19
1.1.2	Performance parameters . . . . .	20
1.1.3	SNSPDs . . . . .	24
1.1.4	SNAPs . . . . .	29
1.2	Thesis outline . . . . .	32
1.2.1	A setup for the characterization of the timing performance of nanowire single-photon detectors . . . . .	33
1.2.2	Timing performance of ultranarrow SNAPs . . . . .	33
1.2.3	Timing performance of SNSPDs . . . . .	33
1.2.4	Vortices in two-dimensional superconductors . . . . .	34
<b>2</b>	<b>Photodetection delay: experimental setup and methods</b>	<b>35</b>
2.1	The instrument response function . . . . .	35
2.2	Experimental specifications to be considered . . . . .	37
2.2.1	Optical setup . . . . .	37
2.2.2	Electronic bandwidth and noise . . . . .	38
2.2.3	Number of samples and integration time . . . . .	39
2.2.4	Sampling resolution . . . . .	40
2.3	Experimental setup . . . . .	41
2.3.1	Jitter of experimental setup . . . . .	42
2.4	Photodetection timeline and measurement procedure . . . . .	44

<b>3</b>	<b>Photodetection delay in ultra-narrow SNAPs</b>	<b>47</b>
3.1	IRF in avalanche regime . . . . .	48
3.1.1	MLD . . . . .	48
3.1.2	Timing jitter . . . . .	51
3.1.3	IRF asymmetry . . . . .	52
3.2	IRF in arm-trigger regime . . . . .	52
<b>4</b>	<b>Photodetection delay in SNSPDs</b>	<b>55</b>
4.1	The instrument response function . . . . .	55
4.1.1	MLD . . . . .	55
4.1.2	Timing jitter . . . . .	58
4.1.3	IRF asymmetry . . . . .	59
4.2	Mathematical interpretation . . . . .	59
<b>5</b>	<b>Current flow and critical current in presence of a vortex in a superconducting strip</b>	<b>65</b>
5.1	3D superconductor . . . . .	66
5.1.1	Surface energy: type I vs type II superconductor . . . . .	66
5.1.2	Modified second London equation: fields and currents of bulk-superconductor vortices . . . . .	68
5.1.3	Vortex near bulk-superconductor boundary . . . . .	71
5.2	2D superconductor . . . . .	72
5.2.1	Vortex in thin superconducting strip . . . . .	73
5.2.2	Photon-assisted vortex tunneling and possible implications for photodetection delay . . . . .	76
<b>6</b>	<b>Summary and outlook</b>	<b>79</b>
6.1	Timing performance of ultranarrow SNAPs . . . . .	79
6.2	Timing performance of SNSPDs . . . . .	80
6.3	Vortex-assisted photon counts . . . . .	81

# List of Figures

1-1	Conceptual difference between a photodiode and a single-photon detector. A regular photodiode requires many photons to generate a photodetection signal. In contrast, the energy of a single photon is sufficient to generate a photodetection signal in a single-photon detector.	20
1-2	Influence of dead time on photodetection. A detected photon results in a photodetection pulse. However, within a time frame $\tau_d$ after the first photon is detected, other photons incident on the detector will not generate additional photodetection pulses.	21
1-3	Influence of limited detection efficiency on photodetection. Not every photon incident onto the detector generates a photodetection pulse.	22
1-4	Influence of timing jitter on photodetection. The time delay between the absorption of a photon in the detector and the generation of a photoresponse varies. The variation is characterized by the timing jitter.	22
1-5	Spectral range and characteristics of common single-photon detector technologies.	23
1-6	Top-down scanning-electron micrograph (SEM) of an SNSPD based on 70-nm-wide nanowires. The inset shows a magnified SEM of the nanowires.	24

1-7	Sketch of photodetection process inside a current-biased superconducting nanowire according to the hotspot model. (a) A photon is absorbed in the nanowire, creating a resistive region (hotspot). (b) The side walks around the hotspot become resistive as a result of current redistribution in the nanowire. (c) Joule heating results in a growth of the resistive region. (d) The resistive region eventually cools down and returns to the superconducting state. . . . .	26
1-8	Simple circuit model for an SNSPD after photon absorption (open switch). The impedance of the readout electronics is modeled with the load resistor $R_L = 50\Omega$ . The inductor in series models the kinetic inductance of the SNSPD. . . . .	26
1-9	Detection efficiency vs. normalized bias current of SNSPDs based on 30-nm-wide nanowires illuminated with 1550-nm-wavelength light, as outlined in Ref. [25]. The bias current of both detectors is normalized by the critical current of the less constricted detector (red curve). . .	28
1-10	Circuit model of a 3-SNAP biased above avalanche current $I_{AV}$ . (a) All three sections are biased at $I_B/3$ . (b) The absorption of a photon drives one of the SNAP sections (initiating section) into the normal state. (c) The current redistribution drives the remaining sections (secondary sections) into the normal state (avalanche), resulting in a current redistribution into the load and a measurable voltage pulse across $R_L$ . . . . .	29
1-11	Device detection efficiency vs. bias current curves of a 3-SNAP measured at photon fluxes ranging from 0.6 (red curve) to 19 million photons per second (purple curve)[25]. In the avalanche regime, the detection efficiency is independent of the incident photon flux. . . . .	30

1-12	Circuit model of a 3-SNAP biased below $I_{AV}$ . (a) An initial HSN drives the initiating section into the normal state. However, the current redistribution is not sufficient to drive the secondary sections into the normal state. (b, c) A second HSN in a secondary section occurs, triggering an avalanche. . . . .	31
2-1	The instrument response function IRF of a nanowire single-photon detector. The IRF is normalized and shifted in time so that its maximum value (maximum-likelihood-delay MLD) is at $\sim 0$ ps. The timing jitter is defined as the full-width-at-half-maximum of the IRF. The IRF shown here has an exponential tail for time delays longer than the MLD. . .	36
2-2	Influence of rise time of the photodetection pulse on timing jitter. Given a noise $\delta V(t)$ , a larger rise time (a) results in larger timing jitter $\delta t$ , while for a smaller rise time (b) the electrical noise has a smaller effect on timing jitter. . . . .	39
2-3	Influence of sampling resolution on rising edge timing. The incoming signal is shown in blue. Insufficient sampling rate (brown dots) results in a more crude approximation of the rising edge of the incoming signal, which translates into timing jitter $\delta t$ . The timing jitter is reduced with increasing sampling rate (red dots). The distance between two samples is $1/r_s$ . . . . .	41
2-4	Schematic illustration of the experimental setup used to measure the instrument response function. . . . .	42
2-5	(a) Setup used to measure the IRF of the setup in Fig. 2-4 excluding the noise contribution of RF amplifiers connected to the SNSPD. (b) IRF of setup shown in (a) using the Thorlabs diode and two mode-locked lasers with $\lambda = 1.55\mu m$ and $\lambda = 1\mu m$ . (c) IRF of setup shown in (a) using the EOT diode and a mode-locked laser at $\lambda = 2\mu m$ . . .	43

2-6	Schematic representation of instances during the photodetection process. A photon from an optical pulse emitted at $t_0$ is absorbed in the nanowire ( $t_{\text{HSN}}$ ), resulting in a resistive slab along the width of the nanowire ( $t_{\xi}$ ). As a result, the bias current is diverted out of the nanowire and into the load, forming an output voltage pulse across the load resistor (see circuit model in chapter 1). The arrival of this pulse can be detected once the rising edge of the single-photon detector pulse surpasses the trigger level of the oscilloscope at $t_{\text{SPD}}$ . . . . .	45
2-7	(a) Measured voltage pulse (averaged over $\sim 5000$ traces) of a 30-nm-wide 2-SNAP for $I_B$ ranging from $0.99I_{\text{SW}}$ to $0.72I_{\text{SW}}$ . Here the time at which the pulse reached its maximum value ( $t_{\text{max}}$ ) was set to 0 s. (b) Time delay between the 95%-of-maximum and 50%-of-maximum transition (at $t_{\text{SPD}}$ ) of the rising edge of the voltage pulses in (a) as a function of normalized bias current $I_B/I_{\text{SW}}$ . . . . .	46
3-1	IRF (normalized to its maximum) of a 30-nm-wide 2-SNAP at the following bias currents: $I_B / I_{\text{SW}} = 1$ (orange), 0.93 (pink), 0.85 (green), 0.78 (blue), 0.73 (black) and 0.69 (wine). The black arrow indicates the direction of increasing $I_B$ . . . . .	49
3-2	(a) IRFs of a 2-SNAP with marked MLD. The MLD at $I_B / I_{\text{SW}} = 1$ , highlighted in red, was set to 0 seconds. (b) MLD vs. normalized bias current $I_B/I_{\text{SW}}$ extracted from the IRFs shown in (a). . . . .	49

3-3	(a) Simulated time evolution of the current $I_{\text{out}}$ diverted to the read-out resistor by a 2-SNAP after a resistive slab of length $\xi$ is formed in the initiating section (at time $t_\xi$ , here set to 0 s) for $I_B / I_{\text{SW}} = 0.96 - 0.66$ . The kinetic inductance of each section of the 2-SNAP was $L_0 = 13$ nH and the series inductor was $L_S = 130$ nH. Black arrows indicate $t_\xi$ , the time at which $I_{\text{out}}$ reaches its maximum ( $t_{\text{max}}$ ) for $I_B / I_{\text{SW}} = 0.96$ and the corresponding detector peak time ( $t_P$ ). (b) Experimental MLD vs $I_B$ (black squares) and simulated $t_P$ vs $I_B$ (red stars). The values of MLD and $t_P$ for the highest $I_B$ were set to 0 s. . . . .	50
3-4	Jitter of a 2-, 3- and 4-SNAP based on 30-nm-wide nanowires as a function of the normalized bias current $I_B / I_{\text{SW}}$ . The switching currents of the 2-, 3-, and 4-SNAP were 13.2 $\mu\text{A}$ , 17.9 $\mu\text{A}$ , and 27.8 $\mu\text{A}$ respectively. The vertical dashed lines indicate the avalanche currents of the SNAPs. The data for the jitter of 3- and 4-SNAPs biased below $I_{\text{AV}}$ are not shown here since the devices were not operating as single photon detectors. . . . .	51
3-5	IRF asymmetry of an SNSPD and 2-, 3- and 4- SNAPs based on 30-nm-wide nanowires as a function of the normalized bias current ( $I_B / I_{\text{SW}}$ ). The SNAPs were identical to the detectors for which data is shown in Fig. 3-4. The vertical dashed lines indicate the avalanche currents of the SNAPs. . . . .	52
3-6	IRF (normalized to its maximum) of a 30-nm-wide 3-SNAP for $I_B$ ranging from $I_{\text{SW}}$ to $0.52I_{\text{SW}}$ . . . . .	53
3-7	(a) MLD of the 3-SNAP shown in Fig. 3-6. The jumps in the MLD are associated with the transition into the arm-trigger-regime. (b,c) Jitter (b) and IRF asymmetry (c) of a 30-nm-wide 3-SNAP (red, $I_{\text{SW}} = 17.9 \mu\text{A}$ ) and 4-SNAP (blue, $I_{\text{SW}} = 25.6 \mu\text{A}$ ). The jumps in the jitter and asymmetry are associated with the transition into the arm-trigger-regime. . . . .	54

4-1	Instrument response function at different bias currents of an SNSPD based on 85-nm-wide nanowires. The detector was illuminated with $\sim 1550$ -nm-wavelength light. The IRFs were shifted in time so that $MLD = 0$ for $I_B \sim I_{SW}$ . . . . .	56
4-2	(a) MLD vs bias current for a 50-nm-nanowire SNSPD, measured at 3 different wavelengths. (b) Time-dependent output current for a 50-nm-nanowire detector simulated with the 1D-electrothermal model. . . . .	56
4-3	MLD and peak time of a 30-nm-nanowire 2-SNAP (a), a 50-nm-nanowire SNSPD (b) and a 100-nm-nanowire SNSPD (c). . . . .	57
4-4	MLD and peak time of SNSPDs based on 50-nm-wide (a), 85-nm-wide (b) and 100-nm-wide nanowires (c). The MLD is shown for three different wavelengths $\lambda = 1.064\mu\text{m}, 1.55\mu\text{m}$ and $2\mu\text{m}$ . . . . .	58
4-5	(a) Initial condition with photon-generated hotspot compared to the initial condition in the 1D-electrothermal model. (b) Simulated output pulse shape for the 1D (red) and 2D (blue) electrothermal model. . . . .	59
4-6	(a) TJ of an SNSPD based on 100-nm-wide nanowires vs. bias current and wavelength. (b) TJ vs. bias current and nanowire width. (c) TJ at different cold head temperatures, wavelengths and bias currents. . . . .	60
4-7	IRF of SNSPDs based on 50-nm-wide(a), 85-nm-wide (b) and 100-nm-wide nanowires (c) illuminated with $1.064\mu\text{m}$ -, $1.55\mu\text{m}$ - and $2\mu\text{m}$ -wavelength light. The detectors were biased close to the critical current. . . . .	60
4-8	(a) IRF of an SNSPD, based on 30-nm-wide nanowires, at different bias currents illuminated with 1550-nm-wavelength light. (b) Parameters $\sigma$ and $\tau$ as a function of bias current. The parameters were extracted from fitted EMGs to the IRFs shown in (a). . . . .	61
4-9	Fitting parameters $\sigma$ (a) and $\tau$ (b) as a function of bias current and wavelength for an SNSPD based on 100-nm-wide nanowires. . . . .	62
4-10	Fitting parameters $\sigma$ (a) and $\tau$ (b) as a function of bias current and wavelength for an SNSPD based on 85-nm-wide nanowires. . . . .	62

4-11	Exponential fitting parameter $\tau$ for SNSPDs based on 30-, 85- and 100-nm-wide nanowires. $\tau$ is shown at different wavelengths as a function of normalized bias current $I_B/I_{SW}$ , where $I_{SW}$ is the switching current of the corresponding SNSPD. . . . .	63
5-1	As in Ref. [45]. (a) Phase diagram of type I superconductor. (b) Phase diagram of type II superconductor. . . . .	66
5-2	As in Ref. [46]. (a) Magnetic flux density and superelectron density at interface between superconductor and normal metal. (b) Vortices in mixed phase. Red circles illustrate the flux through the vortex core and blue arrows the circulating currents that shield the vortex from the rest of the superconductor. . . . .	67
5-3	As in Ref. [46]. Spatial dependence of magnetic flux density and superelectron density around a bulk-superconductor vortex centered at $r=0$ . . . . .	70
5-4	As in Ref. [45]. Schematic representation of field lines for the current density or magnetic vector potential obtained using the image vortex method to solve for the fields and currents around a vortex close to the boundary of a superconductor. The solution is only valid for $x > 0$ . . . . .	71
5-5	Vector fields representing the distribution and direction of the current density around a vortex centered at $x = 1$ (a.u.) placed deep within a bulk superconductor (a) and close to the boundary ( $x = 0$ interface) of a bulk superconductor (b). . . . .	72
5-6	Vortex inside a narrow thin superconducting film (grey strip) centered at a distance $x_0$ from the lower edge. . . . .	74
5-7	Vector field representing the surface current solution using 5.25 for the geometry shown in Figure 5-6. . . . .	75
5-8	(a) Surface current density vector field for a narrow-strip vortex calculated with the image method. (b) Surface current density vector field for a narrow-strip vortex calculated from Kogan's function. . . . .	76

5-9 Potential energy of a vortex in a 50-nm-wide superconducting strip as described in Refs. [31, 32]. The energy, normalized by a scaling factor  $\epsilon_0$  [30], is shown for different bias currents. The arrows denote the height of the energy barrier for a vortex crossing. . . . . 77

# List of Tables

1.1 Comparison of performance parameters of different single-photon-detector technologies. Note that some values are estimates. . . . . 23



# Chapter 1

## Introduction

### 1.1 Single-photon detectors

Single-photon detectors have gained popularity in the last years, particularly due to their crucial role in emerging applications such as quantum key distribution [1], quantum computing and simulation [2, 3, 4] and long-distance optical communication [5, 6]. It is therefore important to understand the unique properties and common performance parameters used to characterize single-photon detectors.

#### 1.1.1 Classification

Figure 1-1 illustrates the difference between a single-photon detector and a photodiode. Due to intrinsic noise, a photodiode requires a large number of photons in order to generate a measurable electrical signal. This photodetection signal can be used to estimate the average photon flux over a given time frame (i.e. the optical power), but not the exact number of photons detected. Common examples of photodiodes are silicon, germanium and indium gallium arsenide optical powermeters [7]. In contrast to a common photodiode, the energy of a single photon is sufficient to trigger a measurable response in a single-photon detector. Since every detected photon generates a corresponding signal (e.g. a photodetection pulse), a single-photon detector enables the 'counting' of the exact number of detected photons in a given time frame. Com-

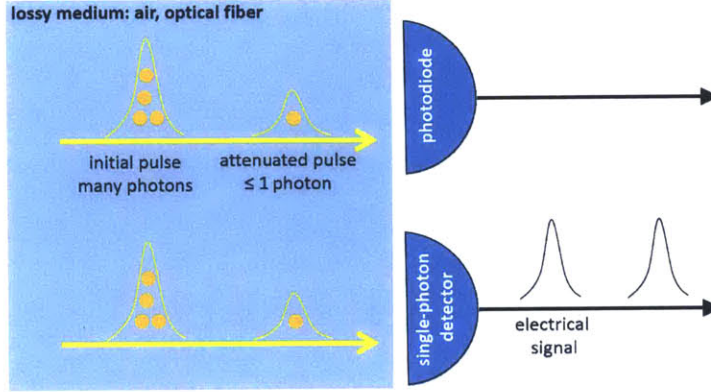


Figure 1-1: Conceptual difference between a photodiode and a single-photon detector. A regular photodiode requires many photons to generate a photodetection signal. In contrast, the energy of a single photon is sufficient to generate a photodetection signal in a single-photon detector.

mon single-photon detectors are photomultiplier tubes (PMT)[8, 9], transition edge sensors (TES)[10], avalanche photodiodes (APD)[11] and superconducting nanowire single-photon detectors (SNSPDs)[12]. The work in this thesis, and therefore the introduction of detector properties and parameters, will focus on SNSPDs.

### 1.1.2 Performance parameters

While the technologies of single-photon detectors differ significantly, there are general metrics that can be used to compare their performance. The main performance parameters are detection efficiency, dark count rate, timing jitter and dead time.

#### Dead time

Figure 1-2 illustrates the effect of a finite dead time  $\tau_d$  in a detector. Within a time window of  $\sim \tau_d$  after initial photodetection, photons incident onto the device do not generate a sufficiently measurable photodetection signal. The detector is therefore 'blind' during the dead time. For a single-channel detector system, the maximum single-photon detection rate (count rate) is limited to  $\sim 1/\tau_d$ .

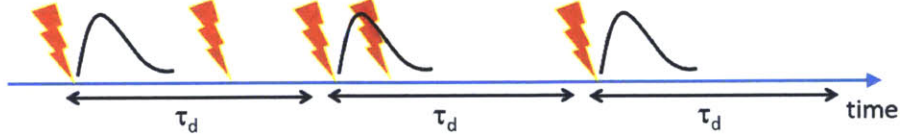


Figure 1-2: Influence of dead time on photodetection. A detected photon results in a photodetection pulse. However, within a time frame  $\tau_d$  after the first photon is detected, other photons incident on the detector will not generate additional photodetection pulses.

### Photon number resolution

Some single-photon detectors, such as the transition edge sensor, exhibit photon number resolution. An optical pulse of the duration  $\tau_p \ll \tau_d$  that contains  $N > 1$  photons incident onto a photon-number-resolving detector will generate a photodetection signal that is modulated according to  $N$ . For a TES,  $N$  can be extracted from the pulse height [13]. Superconducting nanowire single-photon detectors do not intrinsically show photon-number resolution, but effective photon number resolution with SNSPD systems has been demonstrated [14] using multiple independent detectors.

### Detection efficiency

The device detection efficiency ( $\eta$ ) is the probability that a photon incident onto the detector generates a measurable photodetection signal. For practical applications, the system detection efficiency SDE is of interest. The SDE is defined as  $SDE = \eta_c \cdot \eta$ , where  $\eta_c$  is the coupling efficiency between the source (e.g. the input port for an optical fiber) and the active area of the detector.

### Timing jitter

The timing jitter (TJ) is the variation of the photodetection time delay (see Fig. 1-4) and is an important metric for timing-sensitive applications, e.g. pulse-position modulation [15] and quantum key distribution (QKD) [16]. The clock rate of an experiment is ultimately limited to  $\sim 1/TJ$  by the timing jitter. Furthermore, the



Figure 1-3: Influence of limited detection efficiency on photodetection. Not every photon incident onto the detector generates a photodetection pulse.

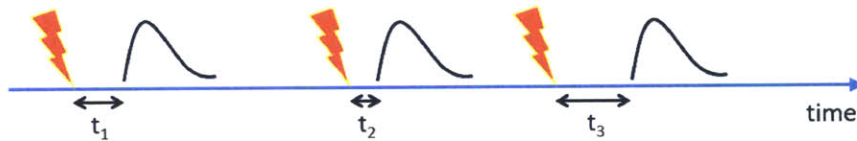


Figure 1-4: Influence of timing jitter on photodetection. The time delay between the absorption of a photon in the detector and the generation of a photoresponse varies. The variation is characterized by the timing jitter.

detector timing jitter limits the secure key exchange rate in QKD [16].

### Specifications of single-photon-detector technologies in comparison

Table 1.1 shows a performance comparison of different single-photon detector technologies.

Detector technology	Detection efficiency (%)	Dark count rate (Hz)	Timing jitter (ps)	Dead time (ns)
PMT [8, 9]	40	100 (vis.), $2 \cdot 10^5$ (IR)	$\leq 30$ (MCP), 300 (IR)	$\leq 100$
TES [8, 10]	95		$10^5$	800
Si-APD (visible) [17]	48	20	30	40
InGaAs-APD (IR) [11]	25	4000 (est.)	67	
WSi-SNSPD [18]	93	1000	150	40
NbTiN-SNSPD [19]	74	100	68	
NbN-SNSPD [20]	74	1000	65-85	4 (est.)

Table 1.1: Comparison of performance parameters of different single-photon-detector technologies. Note that some values are estimates.

For applications that require broadband spectral sensitivity from visible to infrared wavelengths (see Fig. 1-5) or high performance at telecommunication wavelengths, SNSPDs currently offer the best combination of high speed, low timing jitter and high detection efficiency.

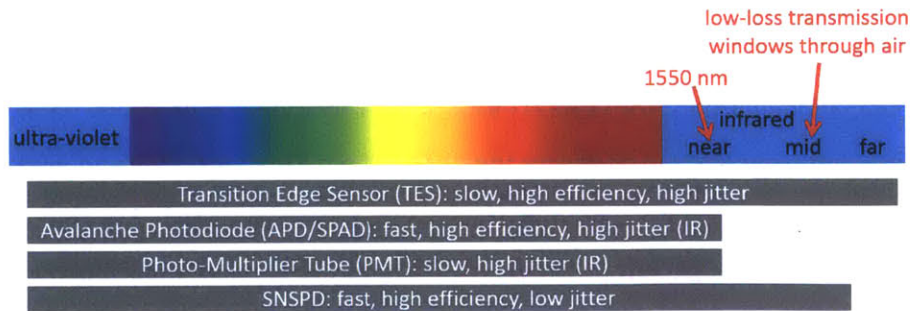


Figure 1-5: Spectral range and characteristics of common single-photon detector technologies.

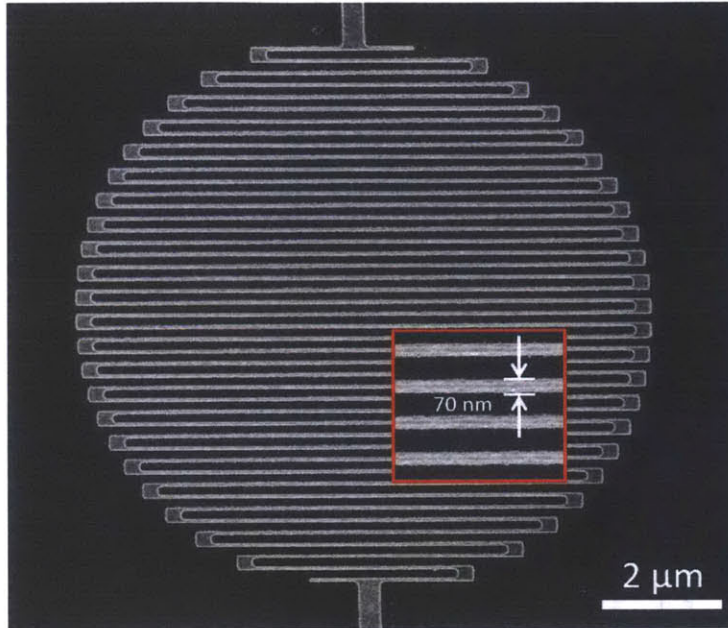


Figure 1-6: Top-down scanning-electron micrograph (SEM) of an SNSPD based on 70-nm-wide nanowires. The inset shows a magnified SEM of the nanowires.

### 1.1.3 SNSPDs

Since their invention in 2001 [12] SNSPDs have emerged as a promising technology for long-distance telecommunication [5, 6] and quantum key distribution [1]. SNSPDs with detection efficiencies up to 93% [21] for 1550nm-wavelength photons, dark count rate of 100 counts per second [19], timing jitter down to 18 ps [22] and wideband spectral sensitivity between UV and mid-IR have been demonstrated [23]. The typical structure of an SNSPD is shown in Figure 1-6. The SNSPD consists of narrow ( $<150$  nm) and thin ( $<10$  nm) superconducting nanowires patterned in a meander structure. Common materials used for SNSPDs are niobium nitride (NbN), niobium titanium nitride (NbTiN) and tungsten silicide (WSi). The detectors studied in this thesis are based on  $\leq 100$ -nm-wide NbN nanowires.

## The hotspot model

Fig 1-7 illustrates the events that result in single-photon detection in superconducting nanowires according to the hotspot model. When a photon is absorbed by a cooper pair in the superconducting nanowire, it generates highly-excited quasiparticles (hot electrons [24]). These highly-excited electrons transfer their energy through scattering and break up additional cooper pairs, generating a localized region filled with secondary normal electrons. This normal region is called the hotspot [24]. Fig. 1-7(a) illustrates a photon-generated hotspot nucleation event (HSN) in a superconducting nanowire. For NbN, the hotspot is believed to be  $\sim 30$  nm in diameter for 1550-nm-wavelength photons [25]. The hotspot repels the supercurrent to sidewalls around it, increasing the current density in the sidewalls. If the initial bias current in the nanowire is high enough so that the current density in the side walls surpasses the critical current density  $J_C$ , the sidewalls will switch to the normal state as well, resulting in a resistive slab across the entire width of the nanowire (Fig. 1-7(b)). The resistive region grows in length due to Joule heating (Fig. 1-7(c)). The current is diverted out of the nanowire into the readout electronics (see next section), allowing for the resistive slab to cool (Fig. 1-7(d)) and to return to the superconducting state. At this point the nanowire can detect the next photon.

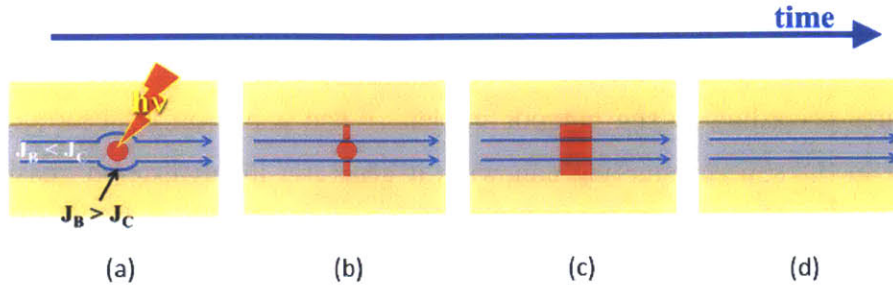


Figure 1-7: Sketch of photodetection process inside a current-biased superconducting nanowire according to the hotspot model. (a) A photon is absorbed in the nanowire, creating a resistive region (hotspot). (b) The side walks around the hotspot become resistive as a result of current redistribution in the nanowire. (c) Joule heating results in a growth of the resistive region. (d) The resistive region eventually cools down and returns to the superconducting state.

### Speed limit and latching

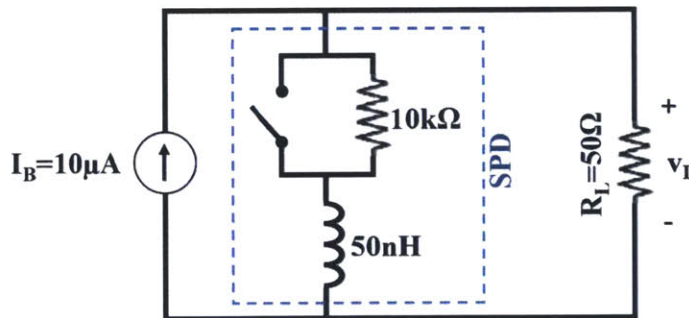


Figure 1-8: Simple circuit model for an SNSPD after photon absorption (open switch). The impedance of the readout electronics is modeled with the load resistor  $R_L = 50\Omega$ . The inductor in series models the kinetic inductance of the SNSPD.

A simplified lumped-element circuit model for an SNSPD is shown in Fig. 1-8. The speed of current dynamics in the detector is limited by the kinetic inductance  $L_K$  [26] of the superconducting wire, which is significantly larger than its geometric inductance. The kinetic inductance limits the current recovery time  $\tau$  from the load

into the detector to  $\tau \sim L_K/50\Omega$ . The dead time of SNSPDs (sometimes referred to as reset time) can be estimated as  $\tau_d \sim 3 \cdot \tau$  [25]. While qualitatively intuitive, this simplified model can not explain the speed limit of SNSPDs due to a stable resistive slab - a behavior referred to as latching. A more advanced approximation is the electrothermal (ET) model, a macroscopic model that quantitatively describes the formation of a measurable photodetection pulse in the readout circuit, the exponential recovery of the photodetection pulse and latching. The ET model for SNSPDs was first introduced by Yang et al. [27]. It is based on two coupled equations. The first equation is the time-dependent heat equation

$$J^2\rho + \kappa\frac{\partial^2 T}{\partial x^2} - \frac{\alpha}{d}(T - T_{\text{sub}}) = \frac{\partial cT}{\partial t} \quad (1.1)$$

and describes the thermal dynamics of the resistive region governed by Joule heating ( $J^2\rho$ , where  $\rho$  is the NbN resistivity), cooling through diffusion inside the NbN ( $\kappa$  is the thermal conductivity of NbN and  $c$  is the specific heat of NbN) and cooling through the substrate ( $\alpha$  is the thermal conductivity between NbN and the substrate). The second equation is the differential equation for the circuit shown in Fig. 1-8 [27]. Both equations are coupled through the time-dependent detector resistance  $R(t)$ . While now frequently used in the field to model the behavior of SNSPDs, the model described here has several shortcomings, which we will discuss later.

## Detection efficiency

Fig. 1-9 shows the detection efficiency vs. bias current of SNSPDs based on 30-nm-wide nanowires. In sub-50-nm-wide SNSPDs based on NbN [25] and in WSi SNSPDs [21], it is generally observed that when illuminated with 1550-nm-wavelength light, at low bias currents  $I_B$  the detection efficiency  $\eta$  increases with  $I_B$  while at high bias currents the detection efficiency reaches a plateau where  $\eta$  shows a small dependence on  $I_B$ . A detection efficiency curve that reaches a plateau is sometimes referred to as saturated. Saturated detectors are a sign of high internal efficiency [28, 21]. Non-

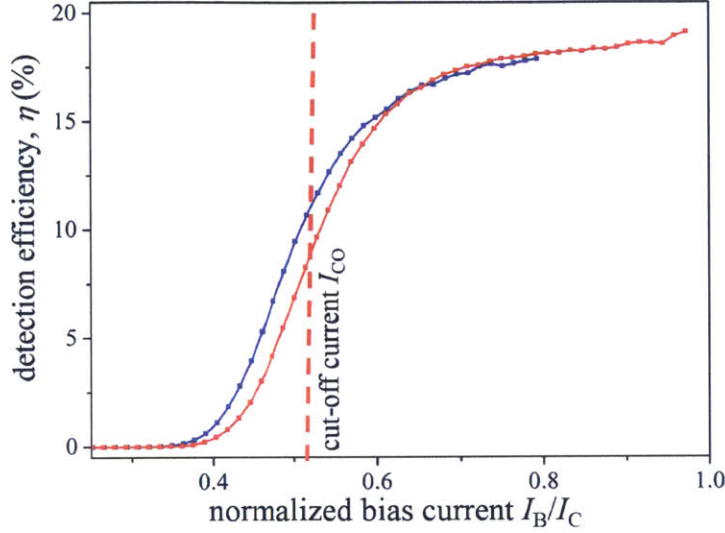


Figure 1-9: Detection efficiency vs. normalized bias current of SNSPDs based on 30-nm-wide nanowires illuminated with 1550-nm-wavelength light, as outlined in Ref. [25]. The bias current of both detectors is normalized by the critical current of the less constricted detector (red curve).

uniformities and defects along the nanowire introduced by the fabrication or film growth processes limit the switching current of the detector, resulting in reduced detection efficiency [29]. Geometries (ultra-narrow nanowires) and materials (WSi and high-quality NbN) that yield saturated detectors are more robust towards constrictions: the purple curve in Fig. 1-9 shows a constricted 30-nm-nanowire SNSPD. Due to a large saturation plateau, the constricted detector can still reach an efficiency value comparable to a less constricted detector (red curve in Fig. 1-9). The inflection point of the  $\eta$  vs.  $I_B$  curve is referred to as cutoff current  $I_{CO}$ .

### Beyond the hotspot model

The simple hotspot model (also referred to as the normal core model), while intuitive, is not sufficient to describe many properties of SNSPDs. Among them is the shape of the detection efficiency vs. bias current curve (see Fig. 1-9): around the cutoff current  $I_{CO}$  the photon count rate strongly depends on bias current, while at high bias currents the detection efficiency curve is flat for high-energy photons or narrow nanowires.

More recently alternative mechanisms have been investigated [30, 31, 32, 33] that yield promising results, especially regarding the photon-energy-dependence of cutoff currents and bias-current-dependence of photon count rates. These models assume the resistive barrier to be (fully or in part) due to the crossing of a vortex. We will discuss vortices as well as some aspects of these models in chapter 5.

### 1.1.4 SNAPs

Superconducting nanowire avalanche photodetectors (SNAPs, also referred to as cascade switching superconducting single photon detectors) [34] are based on a parallel-nanowire architecture that allows single-photon counting with higher signal to noise ratio (SNR, up to a factor of  $\sim 4$  higher [25]) than SNSPDs.

#### The avalanche regime

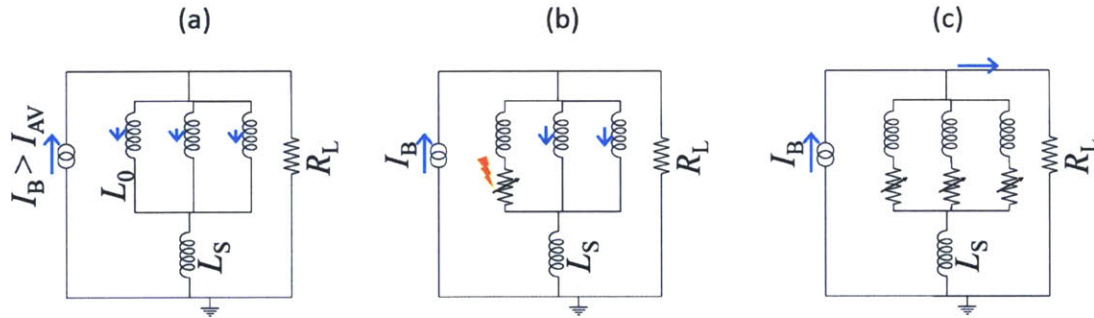


Figure 1-10: Circuit model of a 3-SNAP biased above avalanche current  $I_{AV}$ . (a) All three sections are biased at  $I_B/3$ . (b) The absorption of a photon drives one of the SNAP sections (initiating section) into the normal state. (c) The current redistribution drives the remaining sections (secondary sections) into the normal state (avalanche), resulting in a current redistribution into the load and a measurable voltage pulse across  $R_L$ .

Figure 1-10 illustrates the operation of SNAPs. In the equilibrium state (Fig. 1-10(a)) all  $N$  sections are biased at  $I_B/N$ . The detection event begins with the absorption of

a photon in one of the SNAP sections, shown in Fig. 1-10(b). This section, referred to as initiating section, becomes resistive, diverting its current to the nanowires that are electrically connected in parallel to it. These sections are called secondary sections. If the initial bias current ( $I_B$ ) of a SNAP with  $N$  parallel sections (called N-SNAP) is higher than the avalanche threshold current ( $I_{AV}$ ), the current diverted to the  $(N - 1)$  secondary sections is sufficient to switch these sections to the normal state (Fig. 1-10(c)). We call this process an avalanche. As a result, a current  $\approx N$ -times higher than the current through an individual section is diverted to the read out [34]. In avalanche regime the SNAPs operate as single-photon detectors, i.e. a single hotspot nucleation event (HSN) is sufficient to trigger an avalanche and therefore a measurable detector pulse.

### The arm-trigger regime

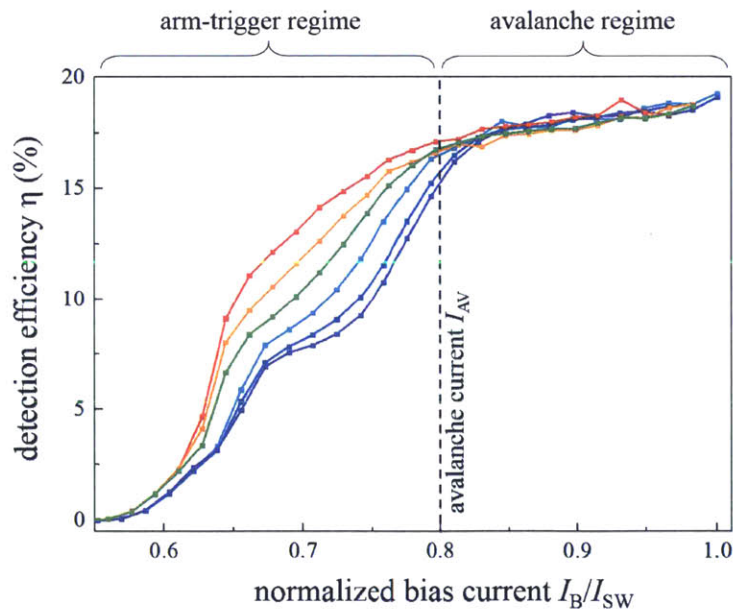


Figure 1-11: Device detection efficiency vs. bias current curves of a 3-SNAP measured at photon fluxes ranging from 0.6 (red curve) to 19 million photons per second (purple curve)[25]. In the avalanche regime, the detection efficiency is independent of the incident photon flux.

When biased below  $I_{AV}$ , the current diverted from the initiating section is not sufficient to trigger an avalanche. For an avalanche to form, additional HSNs have to occur in the secondary sections. Fig. 1-11 shows the detection efficiency vs. bias current-curve for a 3-SNAP [25].

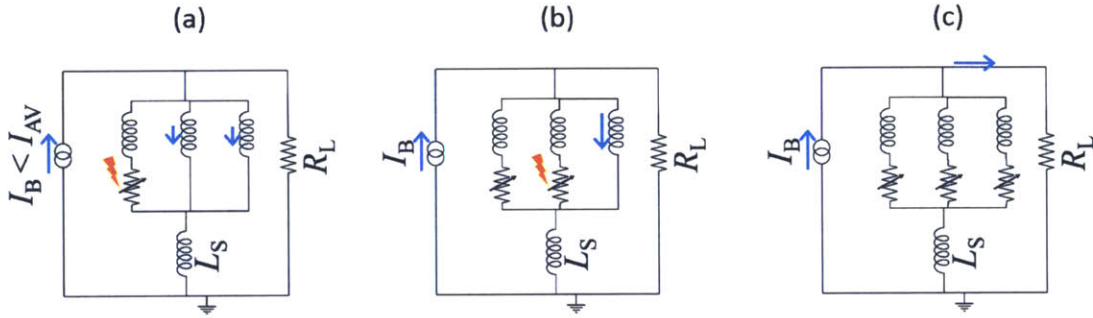


Figure 1-12: Circuit model of a 3-SNAP biased below  $I_{AV}$ . (a) An initial HSN drives the initiating section into the normal state. However, the current redistribution is not sufficient to drive the secondary sections into the normal state. (b, c) A second HSN in a secondary section occurs, triggering an avalanche.

When biased below  $I_{AV}$  at least two HSNs are necessary to trigger an avalanche in this 3-SNAP. We refer to this operation condition as arm-trigger regime, illustrated in Fig. 1-12: the first HSN (Fig. 1-12 (a)) 'arms' the 3-SNAP, activating the remaining two sections. These still-superconducting secondary sections operate as a pseudo-2-SNAP, i.e. they will generate an avalanche if an additional HSN (Fig. 1-12(b)) occurs in one of them. In this regime the SNAP operates as a low-jitter multi-photon gate [35] rather than a single-photon detector. As we will outline in chapter 3, the signature of the arm-trigger regime can be found in the timing performance of SNAPs.

### The unstable regime and afterpulsing

The  $N$  parallel nanowires of an N-SNAP have an  $N^2$ -times lower inductance than an SNSPD with the same area. It was initially believed that the SNAPs have the potential to have an  $N^2$ -times reduced reset time compared to SNSPDs. However,

part of the speed advantage is negated by the choke inductor  $L_S$  in series with the nanowires. We found [36] that a sufficiently large  $L_S$  is essential for stable operation in avalanche regime. A decrease in  $L_S/L_0$  results in an increase in leakage current into the load after the first HSN in the initiating section. The increased leakage current results in an increase of  $I_{AV}$ , i.e. a larger bias current is necessary to trigger an avalanche. A large  $I_{AV}/I_{SW}$  is undesirable because (1) it increases the vulnerability of the detector to noise during operation and (2) it requires the operation of the SNAP in a higher-dark-count rate regime (due to larger bias current). In addition to the undesirable effect of smaller avalanche regime, there is an additional limit on the lowest  $L_S$  value: The reset time of SNAPs in NbN is ultimately limited to  $\geq 1$  ns [36]. SNAPs with smaller reset times showed afterpulsing, i.e. they generated a series of pulses for each detected photon. As a result, in practice the speed limit of SNAPs is similar to SNSPDs ( $\sim 1$  ns, see Ref. [27]).

## 1.2 Thesis outline

The physical origin of the intrinsic timing jitter of detectors based on superconducting nanowires remains unclear after over 10 years since the invention of these detectors. In 2003 Zhang et al. [37] observed a difference in photodetection delay for SNSPDs operating in single-photon regime compared to operation in multi-photon detection regime. The hotspot model eventually failed to explain the observed change in photodetection delay quantitatively. Since the measured change in photodetection delay was on the order of tens of picoseconds, close to the characteristic electron/phonon thermalization times in NbN [24], studying the photodetection delay in SNSPDs offers the potential to probe the photodetection event in time, and therefore to help explain the physics behind single-photon detection in superconducting nanowires. Understanding the photodetection delay could potentially help us engineer detectors with smaller timing jitter, which would enable secure optical communication at higher count rates.

### **1.2.1 A setup for the characterization of the timing performance of nanowire single-photon detectors**

The instrument response function (IRF) will be introduced along with the definitions of MLD and timing jitter. I will discuss the specifications that an experimental setup has to meet in order to enable SNSPD timing jitter measurements with high accuracy. Based on these considerations I will present and characterize the experimental setup used for the measurements in this thesis. Finally, I will describe what time delays were measured and how they relate to different instances during the photodetection process.

### **1.2.2 Timing performance of ultranarrow SNAPs**

I will present the IRF of SNAPs based on 30-nm-wide nanowires as a function of bias current and number of sections. I will show that the correct bias conditions are crucial to achieving low jitter in SNAPs. Furthermore, I will highlight steps in the bias-current-dependence of the IRF parameters. These steps are important indicators marking the different operation regimes of SNAPs, and were historically one of the first indications of these regimes that we observed.

### **1.2.3 Timing performance of SNSPDs**

I will present the IRF of SNSPDs based on 30- to 100-nm-wide nanowires at different wavelengths, to our best knowledge the first systematic study of this kind. These studies will show a surprising width- and wavelength-dependent asymmetry of the IRF, which appears to be not due to the signal-to-noise ratio of the system. I will show that an exponentially-modified Gaussian function fits these IRFs well, with the Gaussian and exponential fitting parameters showing distinct behaviors, which could hint to their connection to two different physical processes.

#### **1.2.4 Vortices in two-dimensional superconductors**

Vortices, of increasing importance for understanding SNSPDs, will be introduced. I will show that a simple image method can be used to calculate the current flow in a superconducting strip in presence of a vortex. This method offers a quick path to calculating current flow in presence of vortices in complex 2-dimensional geometries, e.g. around SNSPD corners and bends. Finally, I will briefly discuss the energy barrier for vortex entry, and possible implications for the shape of the IRFs observed in previous chapters.

# Chapter 2

## Photodetection delay: experimental setup and methods

Measuring the photodetection delay requires an experimental setup with high timing accuracy. In this chapter, we will introduce terminology to describe the time delay response function of nanowire single-photon detectors and discuss the specifications needed for the experimental setup. Based on this discussion we will show a setup with high timing accuracy.

### 2.1 The instrument response function

The timing performance of a single-photon detector can be characterized by measuring the delay between the instant a photon is absorbed in the detector and the instant at which a measurable detector pulse is generated. Figure 2-1 shows a photodetection delay histogram, also called the instrument response function (IRF). The timing jitter (TJ) is defined as the full-width-at-half-maximum (FWHM) of the IRF. The time delay with the largest probability is called maximum-likelihood delay (MLD). In Figure 2-1 the histogram has been shifted in time so that  $MLD=0$ . While mostly Gaussian, some IRFs exhibit an exponential tail, clearly visible when plotted in logarithmic scale. We will use MLD, IRF asymmetry and TJ to quantify the timing performance of SNSPDs and SNAPs. The measured jitter is the convolution of the

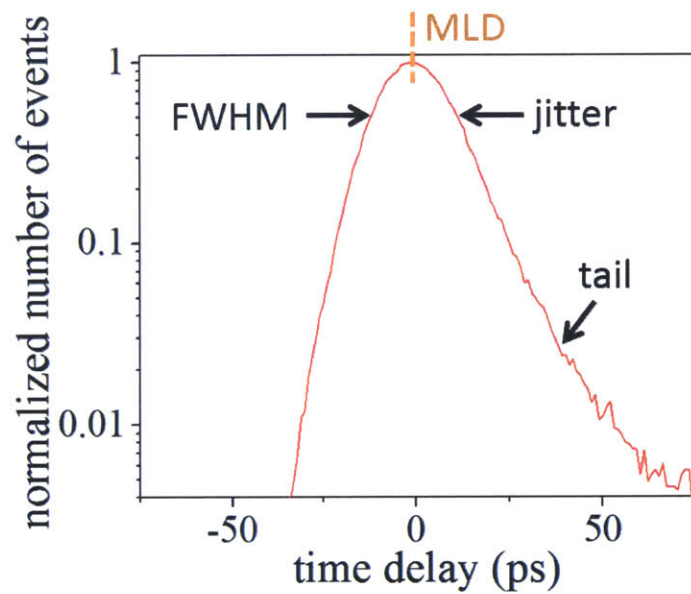


Figure 2-1: The instrument response function IRF of a nanowire single-photon detector. The IRF is normalized and shifted in time so that its maximum value (maximum-likelihood-delay MLD) is at  $\sim 0$ ps. The timing jitter is defined as the full-width-at-half-maximum of the IRF. The IRF shown here has an exponential tail for time delays longer than the MLD.

IRF of the experimental setup and the IRF of the detector. It is therefore important to choose a setup with high timing accuracy and a relatively small influence on the overall shape and width of the measured IRF. We will discuss in the following sections what specifications of the different components of the setup have to be considered in order to design a low-jitter setup.

## 2.2 Experimental specifications to be considered

The timing jitter of the experimental setup  $\Delta t_{\text{setup}}$  limits the measured jitter values  $\Delta t$  to

$$\Delta t = \sqrt{(\Delta t_{\text{setup}})^2 + (\Delta t_{\text{SNSPD}})^2} \quad (2.1)$$

In order to accurately measure the detector jitter  $\Delta t_{\text{SNSPD}}$  it is desirable to keep the setup jitter as small as possible. The main contributions to  $\Delta t_{\text{setup}}$  are from the optical setup, electronic noise and bandwidth, and the accuracy of the timing electronics.

### 2.2.1 Optical setup

In order to measure the photodetection delay, a timing reference is required. A pulsed laser coupled to a fast photodiode and the SNSPD under test provides such a timing reference. Since the timing jitter of SNSPDs is on the order of tens of picoseconds [14], a pulsed laser with a pulse width and pulse-to-pulse jitter (repetition rate stability) on the order of 1 ps should be sufficient. Furthermore, the repetition rate  $f$  of the laser has to be small enough so that

$$f < \frac{1}{\tau_d} \quad (2.2)$$

, where  $\tau_d$  is the dead time of the detector. Since  $\tau_d \leq 10ns$  for the detectors used here,  $f < 100MHz$  is sufficient. A mode-locked pulsed laser can satisfy all the requirements mentioned above. Furthermore, it is important to attenuate the optical power incident onto the detector to  $< 1$  photons per pulse to ensure operation in

single-photon regime [38].

The second component required for a stable timing reference is a fast photodiode. Gbit-rate InGaAs photodiodes can have an internal jitter of  $\leq 3\text{ps}$  and are therefore good candidates. It should be noted that if the optical pulse travels in a medium (i.e. optical fiber), the width increases due to dispersion. Therefore the optical path should be kept short enough so that the pulse width remains on the order of 1 ps at the point of incidence on the photodiode and SNSPD.

## 2.2.2 Electronic bandwidth and noise

Noise from components of the circuit, ground loops, resonances and reflections alter the amplitude  $V_0(t)$  of the ideal noise-free signal to

$$V(t) = V_0(t) + \delta V(t) \quad (2.3)$$

In Fig. 2-2 we compare two pulses: one with a long (Fig. 2-2(a)), the other with a shorter (Fig. 2-2(b)) rise time. In this example a noise  $\delta V(t) = \text{const.}$  is present, translating into a change in the trigger time, and resulting in a jitter  $\delta t$ . The pulse is detected when the rising edge surpasses the trigger level  $V_{\text{tr}} = \text{const.}$  at the time  $t_1$ . This time is different than the detection time  $t_0$  of the ideal pulse and, due to the random nature of the amplitude noise  $\delta V(t)$ , leads to a Gaussian distribution of  $t_1$  around  $t_0$ . The FWHM of the detection time distribution is a source of electronic timing jitter. A high signal-to-noise ratio ensures that

$$\max(|\delta V(t)|) \ll \max(|V_0(t)|) \quad (2.4)$$

and results in smaller electronic jitter (see Figure 2-2(a)). The translation of electronic noise into timing jitter  $\delta t$  also depends on the bandwidth-limited (fast) rising edge of the detector pulse [39]

$$\frac{\delta V(t)}{\delta t} = \frac{V(t) - V_0(t)}{\langle t - t_0 \rangle} \xrightarrow{|\frac{\delta V(t)}{V_0(t)}| \ll 1} \frac{dV(t)}{dt} \Big|_{t_1} \approx \frac{dV_0(t)}{dt} \Big|_{t_1} \Rightarrow \delta t = \frac{\delta V(t)}{\frac{dV_0(t)}{dt} \Big|_{t_1}} \equiv \frac{\delta V(t)}{\nu} \quad (2.5)$$

For a given noise level  $\delta V(t)$ , the jitter decreases as the slope  $\nu$  of the pulse increases, as illustrated in Fig. 2-2(b). Accordingly the bandwidth of the electronics should be high enough to keep the rise time of the pulse as small as possible, ensuring that  $\nu$  is large enough.

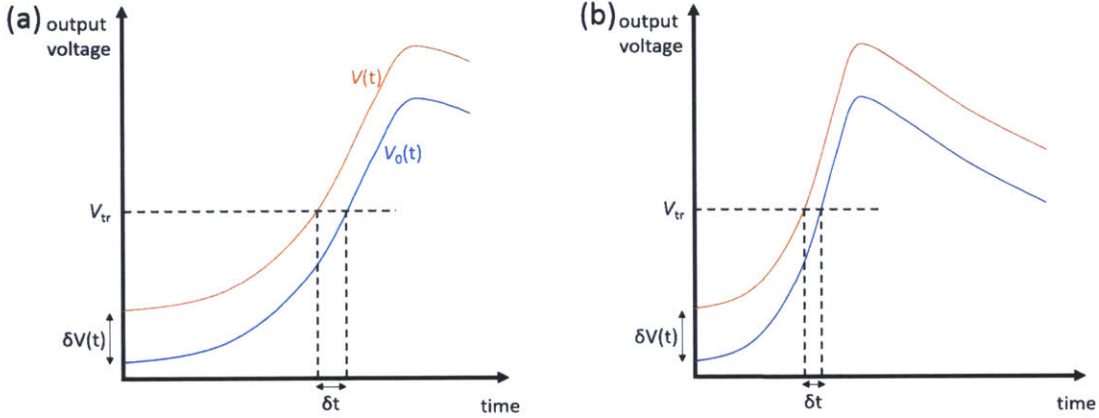


Figure 2-2: Influence of rise time of the photodetection pulse on timing jitter. Given a noise  $\delta V(t)$ , a larger rise time (a) results in larger timing jitter  $\delta t$ , while for a smaller rise time (b) the electrical noise has a smaller effect on timing jitter.

### 2.2.3 Number of samples and integration time

In addition to photodetection delay samples, the IRF also includes a flat background (uncorrelated to the timing reference signal) due to dark counts of the detector. The background limits the minimum number of samples that have to be recorded to resolve details of the IRF (e.g. an exponential tail). Besides actively shielding the detector from stray radiation, there are some strategies that can help reduce the dark count rate (DCR) when recording the IRF. By triggering on the rising (fast) edge of the SNSPD signal and introducing a delay between the SNSPD and reference photodiode (PD) signals, the integration time window can be limited to

$$t_{\text{window}} = \max(t_{\text{rise,SNSPD}}, t_{\text{rise2,PD}}) \quad (2.6)$$

around the rising edge of the SNSPD signal so that the number of background counts per pulse-pair (SNSPD-PD) detection event is limited to  $\sim \text{DCR} \cdot t_{\text{window}}$ . In order to further increase the number of correlated pulse-pair detection events, the incident power should be kept at the highest level at which the SNSPD is still operating in single-photon regime. This power level can be extracted from detection efficiency vs. incident power measurements as illustrated in chapter 1.

## 2.2.4 Sampling resolution

The following properties of the timing electronics (e.g. oscilloscope) affect the timing resolution of the setup: electronic bandwidth, sampling rate (number of voltage samples per second), A/D bit resolution and input noise. The bandwidth of the timing electronics should roughly match the bandwidth of the readout electronics (bias-tee, amplifiers). At a given bandwidth, the accuracy with which the rising edge of a pulse can be resolved is limited by the sampling rate  $r_S$  of the timing electronics, as illustrated in Fig. 2-3. Any inaccuracy in resolving the the rising edge is translated into additional timing jitter. This is the case if

$$r_S \cdot \tau_{\text{rise}} \leq 1 \tag{2.7}$$

, which means that on average only one sample point is taken on the rising edge. The effect of low sampling rate is illustrated in Fig. 2-3(brown trace).

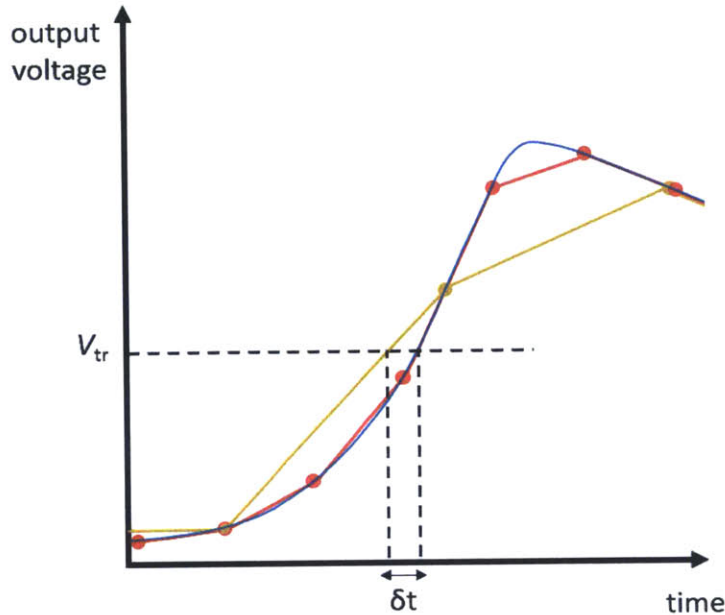


Figure 2-3: Influence of sampling resolution on rising edge timing. The incoming signal is shown in blue. Insufficient sampling rate (brown dots) results in a more crude approximation of the rising edge of the incoming signal, which translates into timing jitter  $\delta t$ . The timing jitter is reduced with increasing sampling rate (red dots). The distance between two samples is  $1/r_s$

As an estimate, at least three sampling points on the rising edge should provide good resolution (see red trace in Fig. 2-3):

$$r_s \cdot \tau_{\text{rise}} \geq 3 \tag{2.8}$$

## 2.3 Experimental setup

A sketch of the experimental setup is shown in Fig. 2-4. The measurements on SNSPDs were performed at three wavelengths of incident light:  $1.064\mu\text{m}$ ,  $1.55\mu\text{m}$  and  $2\mu\text{m}$ . SNAPs were measured using  $1.55\mu\text{m}$ -wavelength light. The detectors were cooled in a cryogenic probe station to  $\sim 2.5\text{K}$  and illuminated with light from

fiber-coupled, mode-locked, sub-5-picosecond-pulse-width lasers (repetition rate  $< 80$  MHz). The laser output was split into two single-mode optical fibers, which we coupled to the detector under test and to a low-jitter fast photodiode (signal rise time  $< 100$  ps, Thorlabs S1R5 and EOT ET-5010F). The signals from the SNSPD and from the fast photodiode were sent to a 6 GHz-bandwidth, 40 GSample/s oscilloscope, which we used to measure the IRF. We verified the operation of the detectors in single-photon regime by setting the power level of the incident light within a range in which the detector photoresponse counts increased linearly with incident power (see chapter 1). We used the following low-noise broadband room-temperature amplifiers to read out the detectors: Miteq AFS5-00100800 (8GHz) for the SNSPDs and Mini-Circuits ZX60-3018G-S+ (3GHz) for the SNAPs.

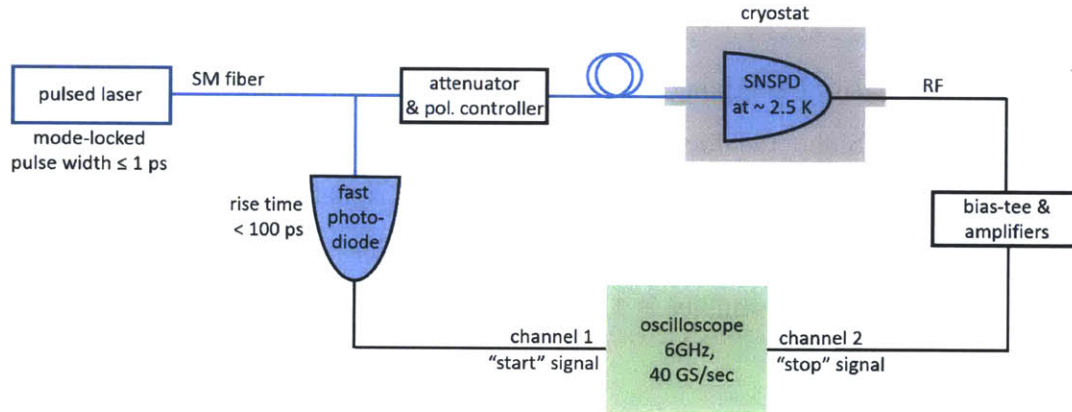


Figure 2-4: Schematic illustration of the experimental setup used to measure the instrument response function.

### 2.3.1 Jitter of experimental setup

We first characterized the timing jitter of the setup. Fig. 2-5(a) shows the experimental setup used to measure the setup IRF. The measured IRF for  $\lambda=1064$ nm and 1550nm is shown in Figure 2-5(b) and the IRF at  $\lambda=2 \mu\text{m}$  is shown in Figure 2-5(c). The fixed oscilloscope trigger level was set to 50% of the average diode pulse amplitude. The IRF for all the laser and diode combinations shown in Figs. 2-5(b,c)

is symmetric - also, note that the IRFs of the Thorlabs diode in (b) for different wavelengths overlap. The FWHM setup jitter of  $\sim 3$  ps includes the following effects:

- Finite laser pulse width
- Pulse-to-pulse jitter of the laser
- Photodiode jitter
- Channel-to-channel timing jitter of the oscilloscope clock
- Timing jitter of the oscilloscope arising from limited sampling rate

However, the setup TJ measured here does not account for the TJ added by amplifiers used to read out the SNSPD.

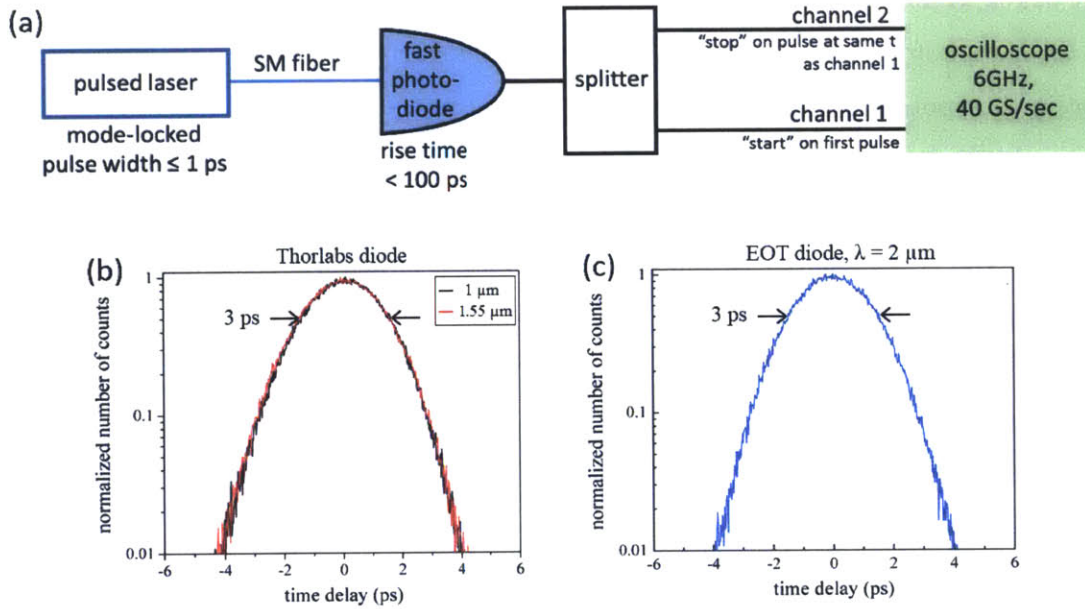


Figure 2-5: (a) Setup used to measure the IRF of the setup in Fig. 2-4 excluding the noise contribution of RF amplifiers connected to the SNSPD. (b) IRF of setup shown in (a) using the Thorlabs diode and two mode-locked lasers with  $\lambda = 1.55\mu m$  and  $\lambda = 1\mu m$ . (c) IRF of setup shown in (a) using the EOT diode and a mode-locked laser at  $\lambda = 2\mu m$ .

## 2.4 Photodetection timeline and measurement procedure

Fig. 2-6 schematically represents the moments [35] of the photodetection process which are relevant to our discussion:

- (1)  $t_0$ : sub-ps laser pulse is emitted;
- (2)  $t_{\text{FPD}}$ : the rising edge of the photoresponse pulse of the fast photodiode reaches 50% of the average pulse peak value;
- (3)  $t_{\text{HSN}}$ : a photon is absorbed in the nanowire and starts a resistive state formation process (hotspot nucleation event HSN);
- (4)  $t_{\xi}$ : the first normal slab of length  $\xi$  (coherence length [40] of the superconductor) is formed across the width of the nanowire;
- (5)  $t_{\text{SPD}}$ : the rising edge of the single-photon detector photoresponse pulse reaches 50% of the average pulse peak value (which depends on  $I_B$ ); and
- (6)  $t_{\text{max}}$ : the single-photon detector pulse reaches its maximum. The IRF is the histogram of a large number of time delay ( $t_D$ ) samples, where  $t_D = t_{\text{SPD}} - t_{\text{FPD}}$ .

We note that the experimental setup shown here does not measure the absolute photodetection delay, but rather the time delay relative to the start signal ( $t_{\text{FPD}}$  in Fig. 2-6)). However, since the length of our RF lines and optical fibers were fixed during the measurements, the offset between the intrinsic time delay and the measured time delay,  $t_{\text{FPD}} - t_0$ , was a constant. As a result this setup allowed us to measure changes in photodetection delay relative to a fixed offset. We fixed the value of this offset by setting the value of the MLD for a detector biased close to its critical current to 0ps.

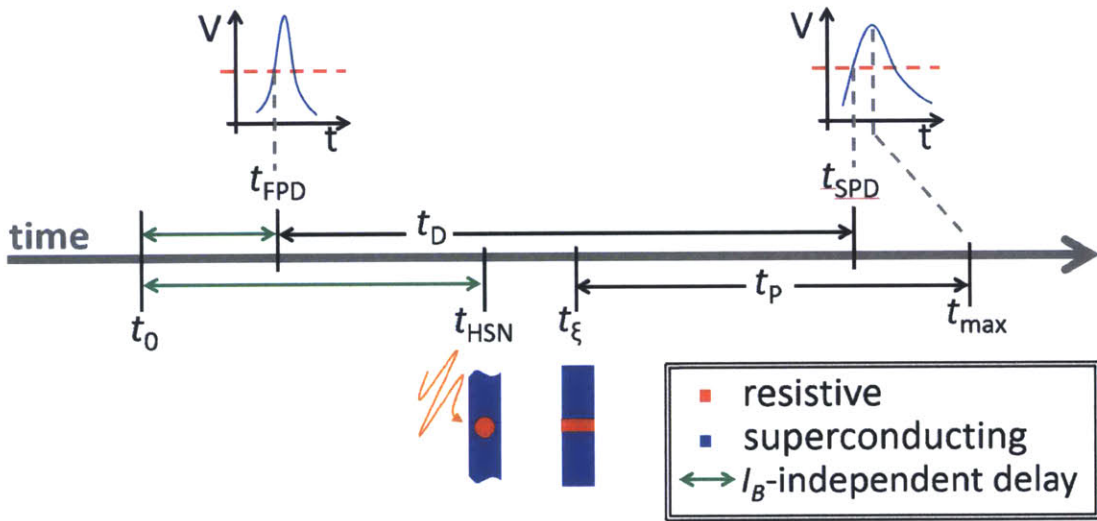


Figure 2-6: Schematic representation of instances during the photodetection process. A photon from an optical pulse emitted at  $t_0$  is absorbed in the nanowire ( $t_{HSN}$ ), resulting in a resistive slab along the width of the nanowire ( $t_\xi$ ). As a result, the bias current is diverted out of the nanowire and into the load, forming an output voltage pulse across the load resistor (see circuit model in chapter 1). The arrival of this pulse can be detected once the rising edge of the single-photon detector pulse surpasses the trigger level of the oscilloscope at  $t_{SPD}$ .

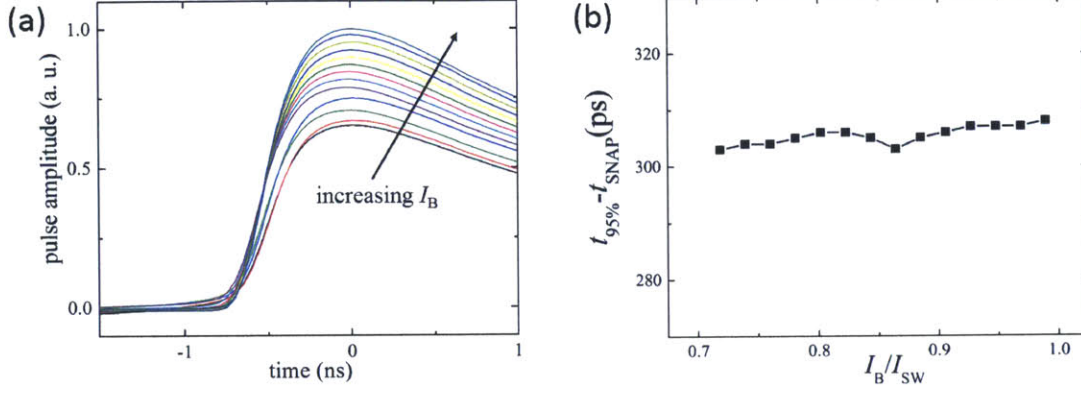


Figure 2-7: (a) Measured voltage pulse (averaged over  $\sim 5000$  traces) of a 30-nm-wide 2-SNAP for  $I_B$  ranging from  $0.99I_{SW}$  to  $0.72I_{SW}$ . Here the time at which the pulse reached its maximum value ( $t_{max}$ ) was set to 0 s. (b) Time delay between the 95%-of-maximum and 50%-of-maximum transition (at  $t_{SPD}$ ) of the rising edge of the voltage pulses in (a) as a function of normalized bias current  $I_B/I_{SW}$ .

The rise time of the measured single-photon detector pulse was limited by the bandwidth of our amplifiers. Experimentally we observed that  $t_{max} - t_{SPD}$  did not vary significantly with  $I_B$ . Figure 2-7 shows the measured averaged voltage pulse of a 2-SNAP at different bias currents. We observed a constant delay ( $\sim 305$  ps) between the times at which the rising edge of the SNAP photoresponse pulse reached 50% and 95% of the peak value ( $t_{SPD}$  and  $t_{95\%}$ ). Here we chose  $t_{95\%}$  instead  $t_{max}$  since  $t_{95\%}$  can be more accurately extracted from the pulse traces. This constant offset between  $t_{SPD}$  and  $t_{95\%}$  allowed us to measure the current-dependent behavior of  $t_{95\%}$  (or equivalently  $t_{max}$ ) by measuring the current-dependent behavior of  $t_{SPD}$  - an essential capability when interpreting the MLD data, as will be shown later in this thesis.

## Chapter 3

# Photodetection delay in ultra-narrow SNAPs

The physical origin of the intrinsic photodetection delay and timing jitter of detectors based on superconducting nanowires remains unclear. Zhang et al. [37] studied the photodetection delay of 130-nm-wide nanowires as a function of power and concluded that the observed 70-ps decrease of photodetection delay between the single-photon and multi-photon regimes might be due to reduced gap suppression time in the multi-photon regime. O'Connor et al. [41] studied the spatial dependence of the photodetection delay and timing jitter (190 - 205 ps) along 100 nm wide nanowires and concluded that narrower nanowire sections have lower delay and jitter. An early study of jitter as a function of wavelength [42] found no significant variation in the range 1 - 2  $\mu\text{m}$  - however, the setup jitter of  $\sim 30$  ps (one order of magnitude larger than for our setup) contributed significantly to the measured jitter of  $\sim 60$  ps, possibly masking the wavelength effect. Along with the dependence on nanowire width, power and photon energy, the bias current dependence may provide decisive insight into the physical origin of photodetection delay and jitter.

Taking advantage of the possibility of efficiently detecting single photons over the entire SNAP bias range with high SNR ( $> 3$ , as defined in Ref. [25]), we studied the timing performance of 30-nm-wide 2-, 3- and 4-SNAPs as a function of the bias current. Our results suggest that, at high bias currents and for narrow nanowires, the

gap suppression time has no dominant effect on the average photodetection delay in the single-photon regime, although it might have an effect on the shape of the IRF. In the following sections we present IRFs of SNAPs with active areas ranging from 0.8 to 2.1  $\mu\text{m}^2$  (see Ref. [25] for details on the fabrication process).

### 3.1 IRF in avalanche regime

We defined the detector IRF as the histogram of the time delay  $t_D$ , with  $t_D = t_{\text{SPD}} - t_{\text{FPD}}$ . The absolute value of  $t_D$  was set by the propagation times of the signals (laser pulse, fast-photodiode pulse and SNAP pulse) through the optical and electrical paths of our set up. These constant paths are marked with green arrows in Fig. 2-6. For the following IRF measurements we added a constant time delay offset so that  $t_D = 0$  s at the maximum of the IRF when the device under test was biased at  $I_B = I_{\text{SW}}$ . We observed two current dependent effects we observed in the IRFs of SNAPs, shown for a 2-SNAP in Fig. 3-1:

- (1) as  $I_B$  was increased, the maximum likelihood delay (MLD) shifted towards shorter time delays;
- (2) as  $I_B$  was lowered, the IRF progressively transitioned from a Gaussian shape (when the detector was biased close to  $I_{\text{SW}}$ ) to a broader and more asymmetric shape with a decaying tail which extended for several hundreds of picoseconds towards longer time delays than the MLD.

#### 3.1.1 MLD

The shift of the MLD to shorter delays with increasing bias current can be explained by considering the time-dependence of the electrothermal dynamics of the devices. Using the electrothermal model described in Ref. [40], we simulated the time evolution of the current diverted from the SNAP to the read-out ( $I_{\text{out}}$ ) after a resistive slab is formed in the initiating section (at time  $t_\xi$ , which we set to 0 s in our simulation). The simulation was performed at different initial values of  $I_B$ . Figure 3-3(a) shows the simulated current pulses from a 2-SNAP. From these pulses we extracted

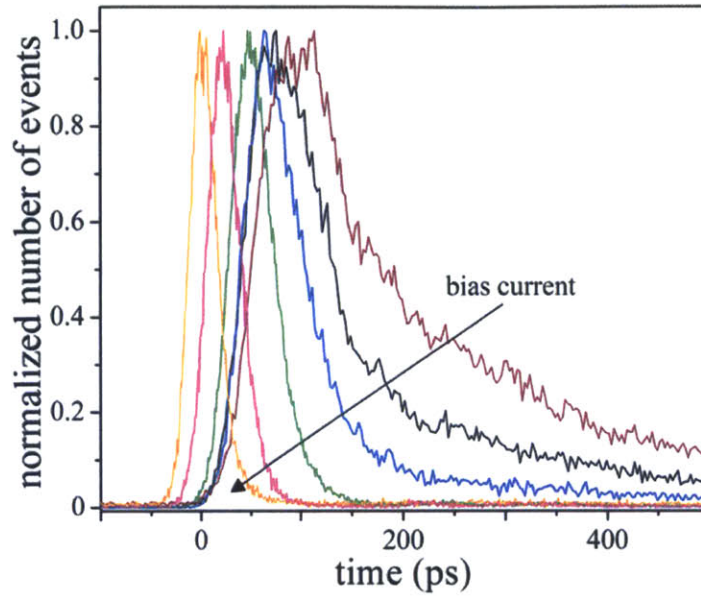


Figure 3-1: IRF (normalized to its maximum) of a 30-nm-wide 2-SNAP at the following bias currents:  $I_B / I_{SW} = 1$  (orange), 0.93 (pink), 0.85 (green), 0.78 (blue), 0.73 (black) and 0.69 (wine). The black arrow indicates the direction of increasing  $I_B$ .

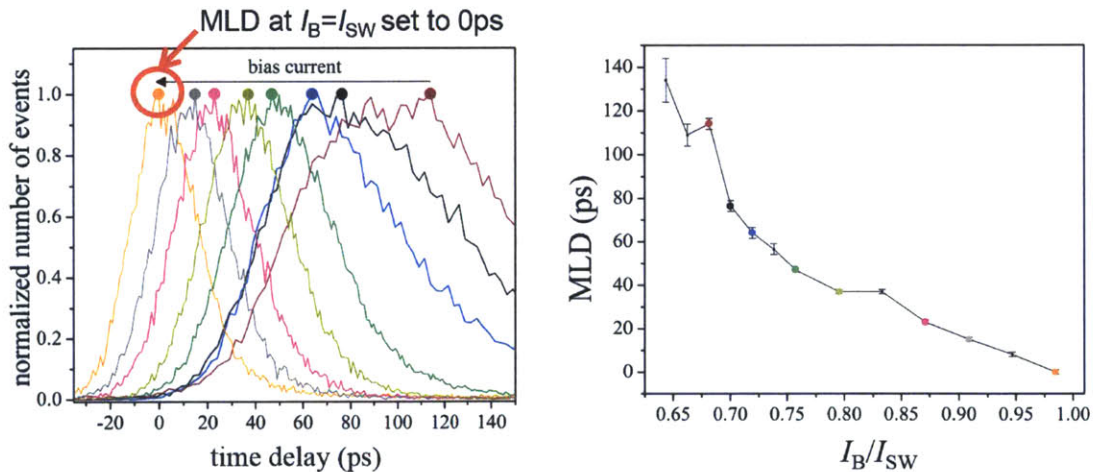


Figure 3-2: (a) IRFs of a 2-SNAP with marked MLD. The MLD at  $I_B / I_{SW} = 1$ , highlighted in red, was set to 0 seconds. (b) MLD vs. normalized bias current  $I_B / I_{SW}$  extracted from the IRFs shown in (a).

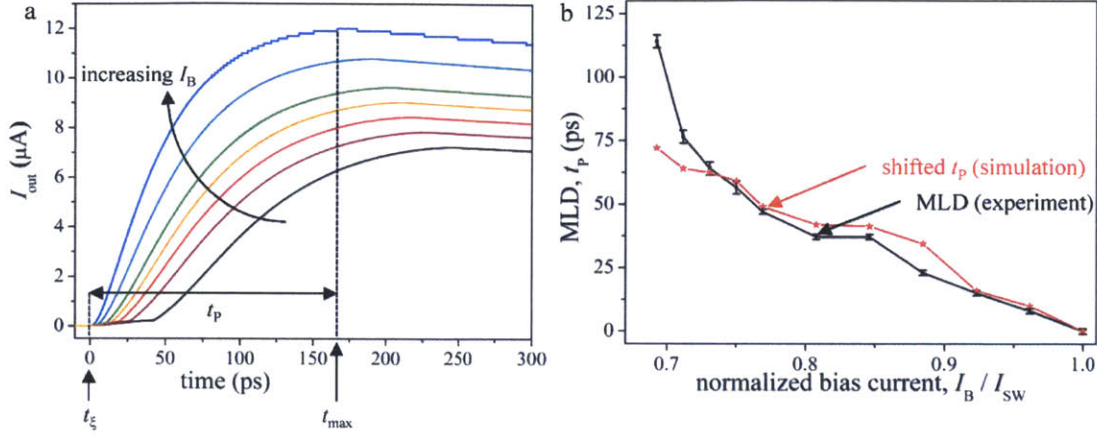


Figure 3-3: (a) Simulated time evolution of the current  $I_{\text{out}}$  diverted to the read-out resistor by a 2-SNAP after a resistive slab of length  $\xi$  is formed in the initiating section (at time  $t_\xi$ , here set to 0 s) for  $I_B / I_{\text{SW}} = 0.96 - 0.66$ . The kinetic inductance of each section of the 2-SNAP was  $L_0 = 13$  nH and the series inductor was  $L_S = 130$  nH. Black arrows indicate  $t_\xi$ , the time at which  $I_{\text{out}}$  reaches its maximum ( $t_{\text{max}}$ ) for  $I_B / I_{\text{SW}} = 0.96$  and the corresponding detector peak time ( $t_P$ ). (b) Experimental MLD vs  $I_B$  (black squares) and simulated  $t_P$  vs  $I_B$  (red stars). The values of MLD and  $t_P$  for the highest  $I_B$  were set to 0 s.

the peak time  $t_P$ , corresponding to  $t_P = t_{\text{max}} - t_\xi$ . After the avalanche, the resistance  $R(t)$  of the SNAP grows with time as a result of the dissipated power proportional to  $R(t) \cdot I_B^2$  (Joule heating). At lower bias currents, the dissipated power is smaller, resulting in a slower increase of  $R(t)$ . Hence it takes longer for the diverted current  $I_{\text{out}}$  to reach its peak value. Figure 3-3(b) shows the shifted  $t_P$  (simulation; defined as  $t_P(I_B) - t_P(I_B = I_{\text{SW}})$ ) and the MLD (experiment) of a 2-SNAP as a function of  $I_B$ . As the shifted  $t_P$  and the MLD are in good agreement, we conclude that the MLD differs at most by a current-independent offset from  $t_P$ . Note that the 1-dimensional electrothermal model used here [40] appears to be a good approximation for devices based on ultranarrow nanowires (here  $\sim 30$ -nm-wide nanowires), which is not necessarily the case for wider nanowires, as we will see in the next chapter.

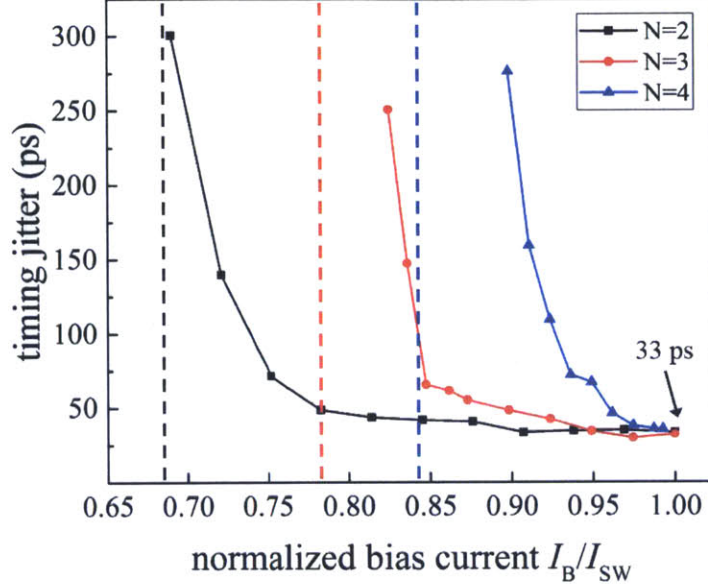


Figure 3-4: Jitter of a 2-, 3- and 4-SNAP based on 30-nm-wide nanowires as a function of the normalized bias current  $I_B / I_{SW}$ . The switching currents of the 2-, 3-, and 4-SNAP were  $13.2 \mu\text{A}$ ,  $17.9 \mu\text{A}$ , and  $27.8 \mu\text{A}$  respectively. The vertical dashed lines indicate the avalanche currents of the SNAPs. The data for the jitter of 3- and 4-SNAPs biased below  $I_{AV}$  are not shown here since the devices were not operating as single photon detectors.

### 3.1.2 Timing jitter

Figure 3-4 shows the jitter of 2-, 3- and 4-SNAPs as a function of the normalized bias current  $I_B / I_{SW}$ . The jitter of SNAPs showed a weak dependence on the bias current for  $I_B$  close to  $I_{SW}$  (e.g. for a 2-SNAP the jitter increased from  $\sim 35$  ps at  $I_B = 0.97I_{SW}$  to 41 ps at  $I_B = 0.88I_{SW}$ ), but rapidly increased as  $I_B$  approached  $I_{AV}$  (by  $\sim 100$  ps for a decrease in  $I_B$  of  $0.1I_{SW}$ ).  $I_{AV}$  was determined from detection efficiency measurements, as reported in Ref. [25]. We note that for  $I_B$  approaching  $I_{SW}$ , SNAPs showed the same jitter as standard SNSPDs ( $\sim 33$  ps [14]), in contrast to previous reports of longer jitter times in SNAPs [43].

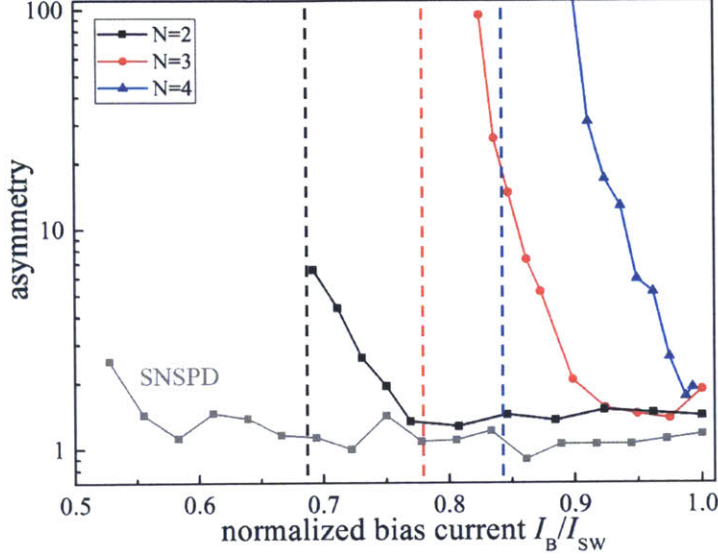


Figure 3-5: IRF asymmetry of an SNSPD and 2-, 3- and 4-SNAPs based on 30-nm-wide nanowires as a function of the normalized bias current ( $I_B / I_{SW}$ ). The SNAPs were identical to the detectors for which data is shown in Fig. 3-4. The vertical dashed lines indicate the avalanche currents of the SNAPs.

### 3.1.3 IRF asymmetry

Figure 3-5 shows the IRF asymmetry, defined as the ratio between the length of the IRF tails (experimentally defined as the time between 90% and 10% of the IRF maximum) after and before the MLD. Like the jitter, the asymmetry of SNAPs showed a weak dependence on the bias current at high  $I_B$ , but rapidly increased as  $I_B$  approached  $I_{AV}$ .

## 3.2 IRF in arm-trigger regime

The behavior of the IRF was one of the first indications of the arm-trigger regime when we studied SNAPs: when biased below  $I_{AV}$ , 3- and 4-SNAPs operated in arm-trigger regime (see chapter 1). In this regime the two or more HSN events (each being a photon count or dark count) was necessary to generate a detector pulse (2 HSN events for 3-SNAPs and 2 or 3 HSN events, depending on the bias current, for 4-SNAPs). While SNAPs do not operate as single-photon detectors in this regime, good timing

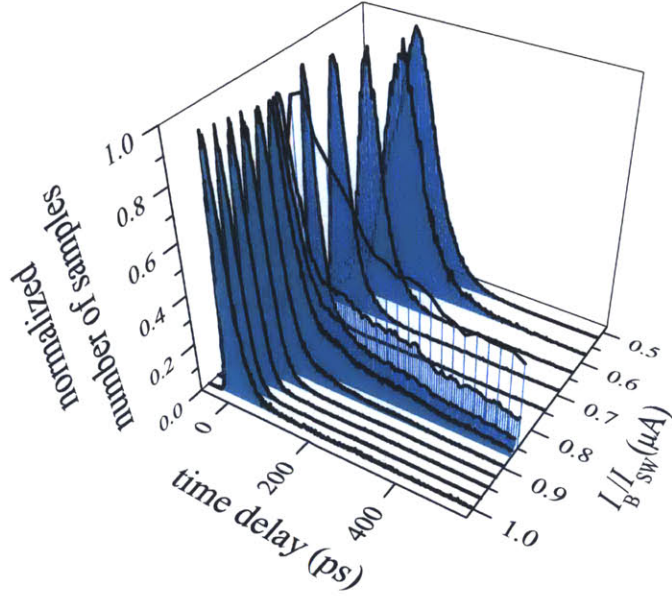


Figure 3-6: IRF (normalized to its maximum) of a 30-nm-wide 3-SNAP for  $I_B$  ranging from  $I_{SW}$  to  $0.52I_{SW}$ .

performance in this regime would possibly make SNAPs attractive for applications that require conditional multi-photon detection (e.g. as an N-photon gate). Figure 3-6 shows the IRF of a 3-SNAP for  $I_B$  ranging from  $0.52I_{SW}$  to  $I_{SW}$ . The IRF became wider and more asymmetric as  $I_B$  was lowered from  $\sim I_{SW}$  to  $I_{AV} \sim 0.8I_{SW}$ . For  $I_B$  slightly below  $I_{AV}$  (arm-trigger regime), the IRF abruptly changed shape and became approximately as narrow and symmetric as the IRF measured in single-photon regime at  $I_B \sim I_{SW}$ . As  $I_B$  was lowered further, the IRF became again wider and more asymmetric.

Figure 3-7 shows a quantitative characterization of the shape of the IRF of 3- and 4-SNAPs in terms of its MLD, width (jitter) and asymmetry. The abrupt changes in the shape of the IRF as a function of  $I_B$  coincide with the transition into multi-HSN regimes that are also observable in the current-dependence of the detection efficiency (see Fig. 1-11).

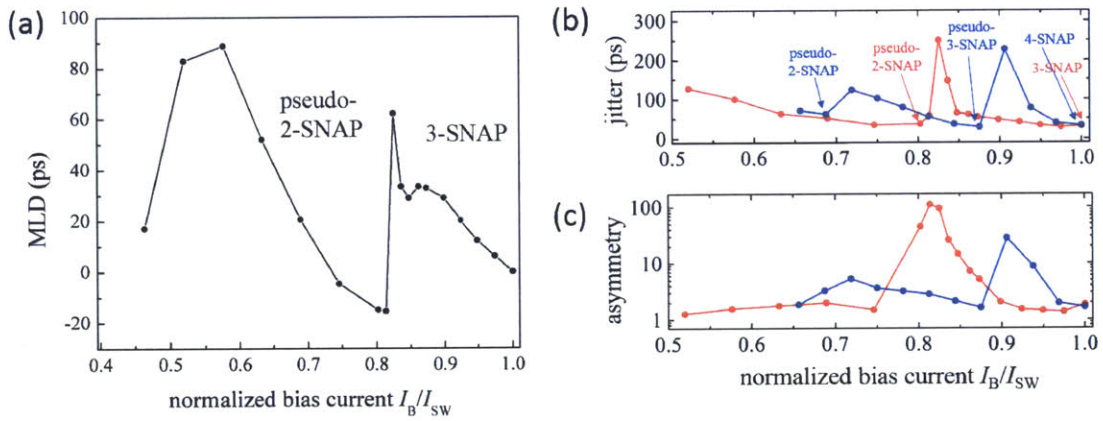


Figure 3-7: (a) MLD of the 3-SNAP shown in Fig. 3-6. The jumps in the MLD are associated with the transition into the arm-trigger-regime. (b,c) Jitter (b) and IRF asymmetry (c) of a 30-nm-wide 3-SNAP (red,  $I_{SW} = 17.9 \mu\text{A}$ ) and 4-SNAP (blue,  $I_{SW} = 25.6 \mu\text{A}$ ). The jumps in the jitter and asymmetry are associated with the transition into the arm-trigger-regime.

# Chapter 4

## Photodetection delay in SNSPDs

While the photoresponse signal of SNAPs is relatively easy to measure due to the high signal-to-noise ratio, measuring the photodetection delay of SNSPDs, which are significantly less complex than SNAPs, can be a more accessible way to studying the photodetection process in superconducting nanowires.

### 4.1 The instrument response function

In a similar approach to our measurements on SNAPs, we recorded the IRF of SNSPDs based on  $\sim 30$ -, 50- and 80- and 100-nm-wide nanowires. We performed the measurements as a function of bias current and at three wavelengths:  $1\ \mu\text{m}$ ,  $1.55\ \mu\text{m}$  and  $2\ \mu\text{m}$ .

Figure 4-1 shows the IRF of an 85-nm-wide SNSPD at different bias currents for  $1.55\ \mu\text{m}$ -wavelength light. The SNSPD IRFs showed a behavior qualitatively similar to SNAPs biased above  $I_{AV}$ .

#### 4.1.1 MLD

Fig. 4-2(a) shows the dependence of the MLD of a 50-nm-nanowire SNSPD on bias current and wavelength. For 30-nm-nanowire SNAPs in Ref. [35] (see previous chapter) we had already demonstrated that the electrothermal model [27] was sufficient to

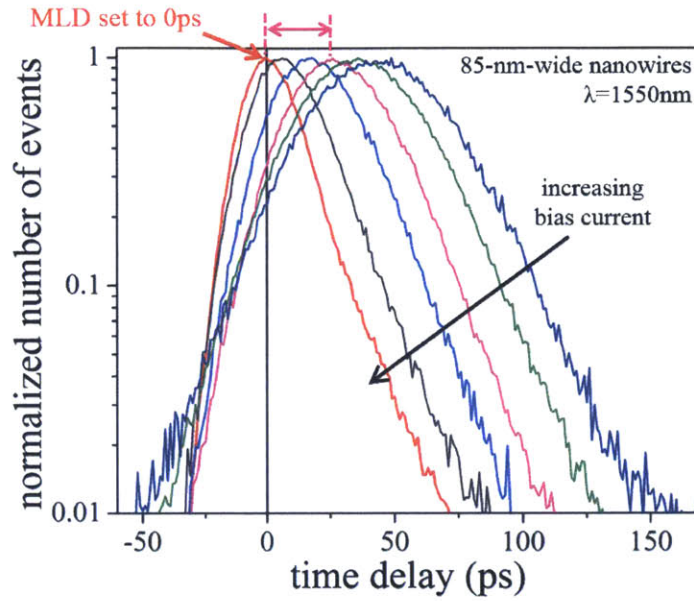


Figure 4-1: Instrument response function at different bias currents of an SNSPD based on 85-nm-wide nanowires. The detector was illuminated with  $\sim 1550$ -nm-wavelength light. The IRFs were shifted in time so that  $MLD = 0$  for  $I_B \sim I_{SW}$

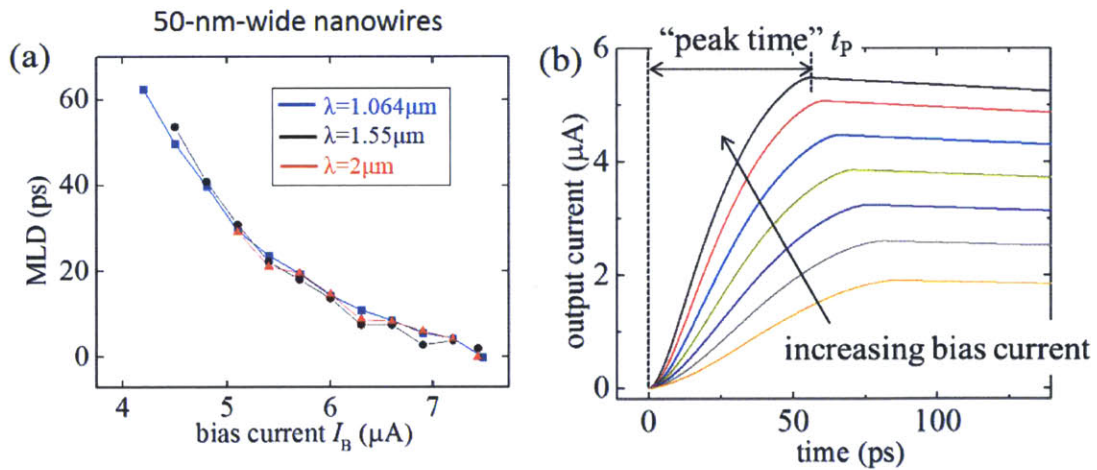


Figure 4-2: (a) MLD vs bias current for a 50-nm-nanowire SNSPD, measured at 3 different wavelengths. (b) Time-dependent output current for a 50-nm-nanowire detector simulated with the 1D-electrothermal model.

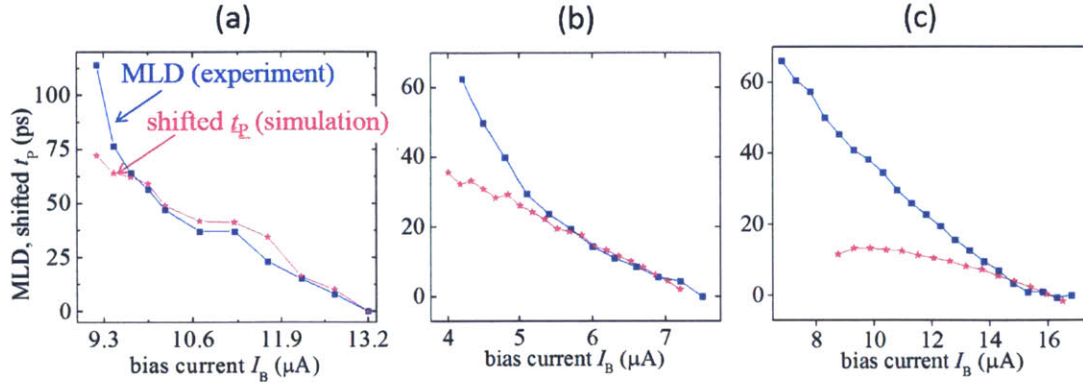


Figure 4-3: MLD and peak time of a 30-nm-nanowire 2-SNAP (a), a 50-nm-nanowire SNSPD (b) and a 100-nm-nanowire SNSPD (c).

describe the MLD, so the lack of the dependence of MLD of SNSPDs on wavelength was not surprising. As outlined in chapter 3, we associated the MLD with the peak time, the time between the instant of photon absorption in the nanowire and the instant at which the output current reaches its maximum value ( $t_P = t_{\max} - t_\xi$ ). The peak time was calculated by simulating the time-dependent output current with the electrothermal model [40, 27]. The results for the 50-nm-nanowire SNSPD are shown in Fig. 4-2(b).

As outlined in the previous chapter, the peak time increases with decreasing bias current due to reduced Joule heating, resulting in a larger peak time. Fig. 4-3 shows the shifted  $t_P$  (simulation; defined as  $t_P(I_B) - t_P(I_B = I_{SW})$ ) and the MLD (experiment) of detectors based on 30-, 50- and 100-nm-wide nanowires. While for 30-nm-wide nanowires the shifted  $t_P$  and the MLD are in good agreement, the 1D-electrothermal model is not sufficient to describe the behavior of the MLD for wider nanowires at low bias currents, which could hint as a shortcoming of the 1-dimensional electrothermal model used here.

In order to develop an improved model for the photodetection delay it is important to understand the approximations made by the electrothermal model [27]:

- (1) The initial condition assumed by the electrothermal model is a normal slab across the nanowire - thus ignoring any initial process that led to the creation of the slab. While this assumption may be a good approximation for ultranarrow nanowires, as

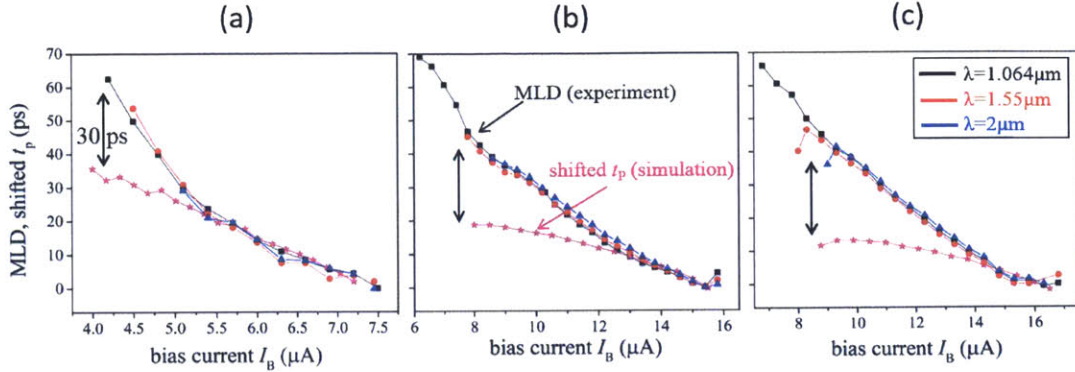


Figure 4-4: MLD and peak time of SNSPDs based on 50-nm-wide (a), 85-nm-wide (b) and 100-nm-wide nanowires (c). The MLD is shown for three different wavelengths  $\lambda = 1.064 \mu m, 1.55 \mu m$  and  $2 \mu m$ .

illustrated in Figure 4-5(a), it might be a more crude approximation for the photodetection dynamics in wider nanowires.

(2) The electrothermal model used here is a one-dimensional model, therefore ignoring any two-dimensional current dynamics or spatial non-uniformities of nanowire temperature caused by the absorption of a photon (see Fig. 4-5(a)).

(3) The electrothermal model does not include the effect of gap suppression time [44, 43], which could result in larger photodetection delay at low bias currents.

As illustrated in Fig. 4-5(b), the approximations outlined above result in an underestimation of the rise time or peak time of the detector pulse (see first observation in Ref. [27]), which could explain the discrepancy between the current-dependent behavior of  $t_p$  and the MLD. An improved 2-dimensional model should be based on a two-temperature model, as outlined in the supplementary information of ref. [40], and include the time-dependent effects of temperature on the superconducting gap (e.g. see ref. [32]).

### 4.1.2 Timing jitter

The FWHM timing jitter appeared to have only a very weak dependence on wavelength (Fig. 4-6(a)) and no dependence on temperature 4-6(c) at a given bias current, indicating that the main contribution to timing jitter is the signal-to-noise ratio.

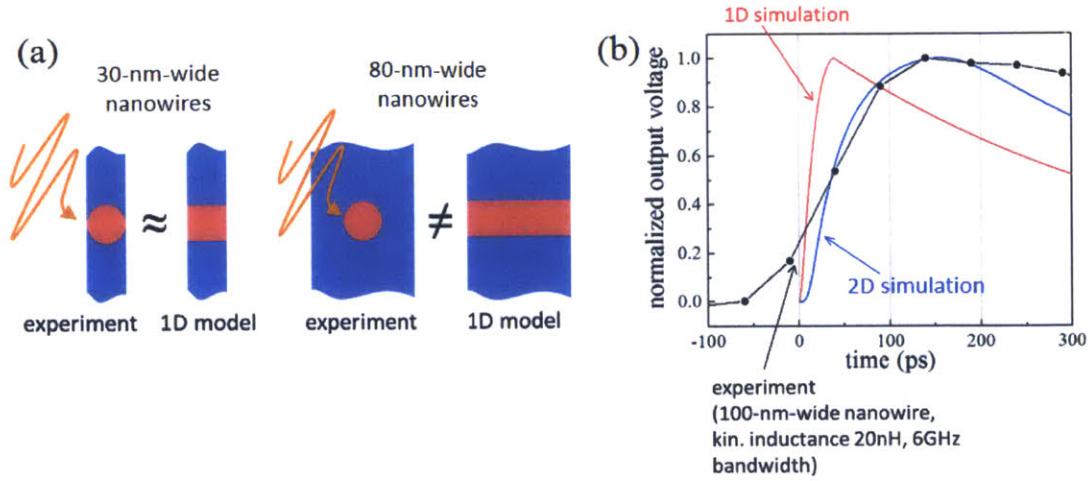


Figure 4-5: (a) Initial condition with photon-generated hotspot compared to the initial condition in the 1D-electrothermal model. (b) Simulated output pulse shape for the 1D (red) and 2D (blue) electrothermal model.

Therefore increasing the signal amplitude should help reduce timing jitter.

## 4.2 IRF asymmetry

The asymmetric tail, shown in Fig. 4-7, was the only feature of the IRF that showed a significant dependence on wavelength. For a given bias current, the observed asymmetry increased with increasing wavelength and width. This dependence on energy implies that the initial hotspot size or gap suppression time could play a role here.

## 4.3 Mathematical interpretation

We found that the IRFs of SNSPDs could be fitted with an exponentially-modified Gaussian (EMG), defined as the convolution

$$EMG(t) = \left( A \cdot \exp\left(-\left(\frac{x}{\sigma}\right)^2\right) * \exp\left(-\frac{y}{\tau}\right) \right) (t) \quad (4.1)$$

Figure 4-8 (a) shows the IRFs of an SNSPD based on 30-nm-wide nanowires at different bias currents ( $\lambda = 1.55\mu\text{m}$ ). For ease of illustration the IRFs were shifted in

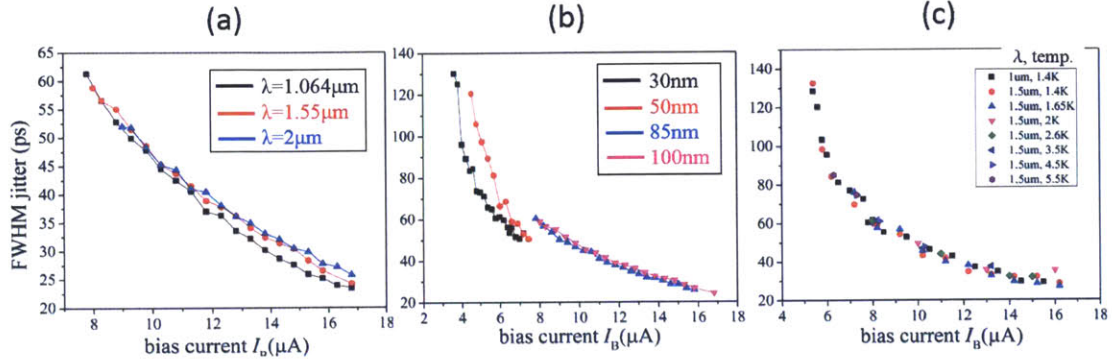


Figure 4-6: (a) TJ of an SNSPD based on 100-nm-wide nanowires vs. bias current and wavelength. (b) TJ vs. bias current and nanowire width. (c) TJ at different cold head temperatures, wavelengths and bias currents.

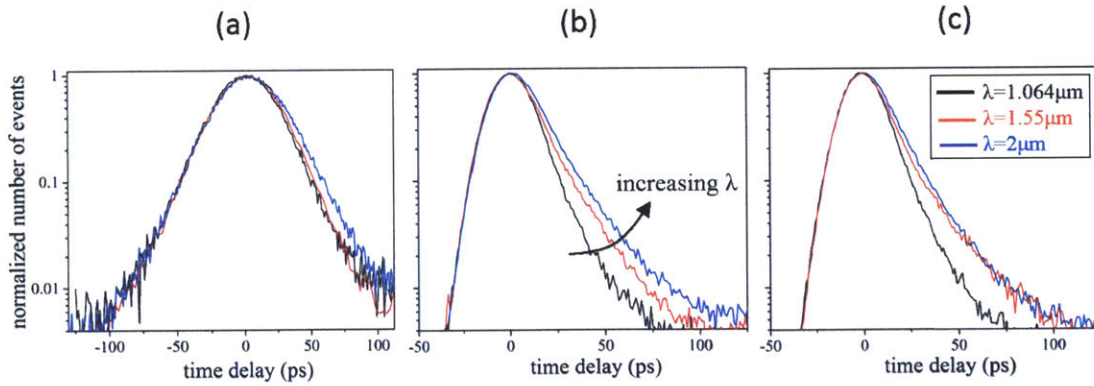


Figure 4-7: IRF of SNSPDs based on 50-nm-wide (a), 85-nm-wide (b) and 100-nm-wide nanowires (c) illuminated with  $1.064 \mu\text{m}$ -,  $1.55 \mu\text{m}$ - and  $2 \mu\text{m}$ -wavelength light. The detectors were biased close to the critical current.

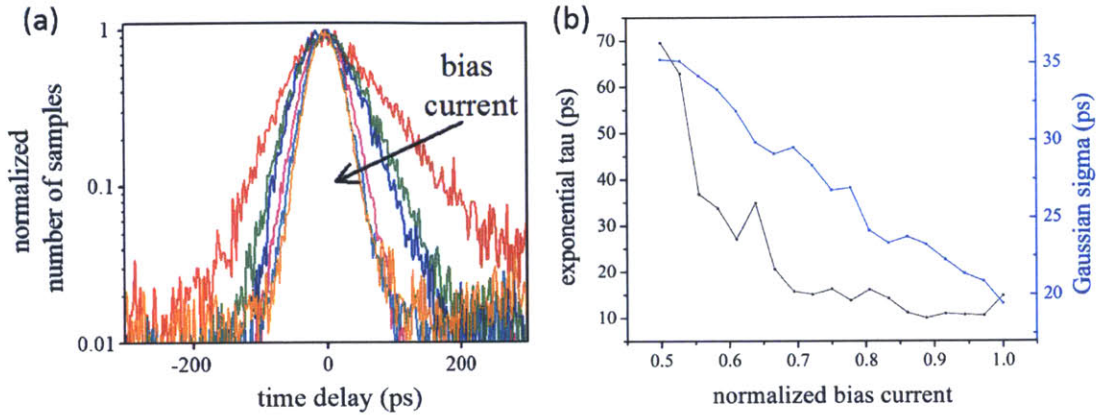


Figure 4-8: (a) IRF of an SNSPD, based on 30-nm-wide nanowires, at different bias currents illuminated with 1550-nm-wavelength light. (b) Parameters  $\sigma$  and  $\tau$  as a function of bias current. The parameters were extracted from fitted EMGs to the IRFs shown in (a).

time to  $t=0$ . Each IRF was fitted to an EMG. The fitting parameters (exponential  $\tau$  and Gaussian  $\sigma$ ) are shown in Fig. 4-8 (b). While  $\sigma$  shows a clear linear dependence over the entire bias current range,  $\tau$  appears to vary little at high bias currents. The asymmetry increases as the bias current approaches the cutoff current  $I_{CO}$ , similar to the behavior of SNAPs for currents close to the avalanche current  $I_{AV}$ . However, in contrast to SNSPDs, the IRFs of SNAPs could not be fitted well with an EMG, partially due to the more complex shape of their asymmetric tail.

Figure 4-9 shows the dependence of  $\sigma$  and  $\tau$  on bias current and wavelength. While  $\sigma$  shows no wavelength-dependence,  $\tau$  appears to approach a plateau with decreasing photon energy. The distinct behavior of  $\sigma$  and  $\tau$  suggest that these features of the IRF could be a signature of two separate physical effects. The wavelength-independence of  $\sigma$  and its increasing values at low bias currents suggest that the major contribution to  $\sigma$  arises from electrical noise.

The  $\sim 13$ -ps-plateau is observed across several detectors, bias currents and wavelengths, as shown in Fig. 4-11. The IRF approaches the plateau at (1) lower bias currents and (2) lower photon energies. We conclude that  $\tau$  could be related to the initial stages of photon absorption (hotspot, vortex dynamics, gap suppression time): In regime (1) the effect of joule heating to the initial creation of the resistive slab is

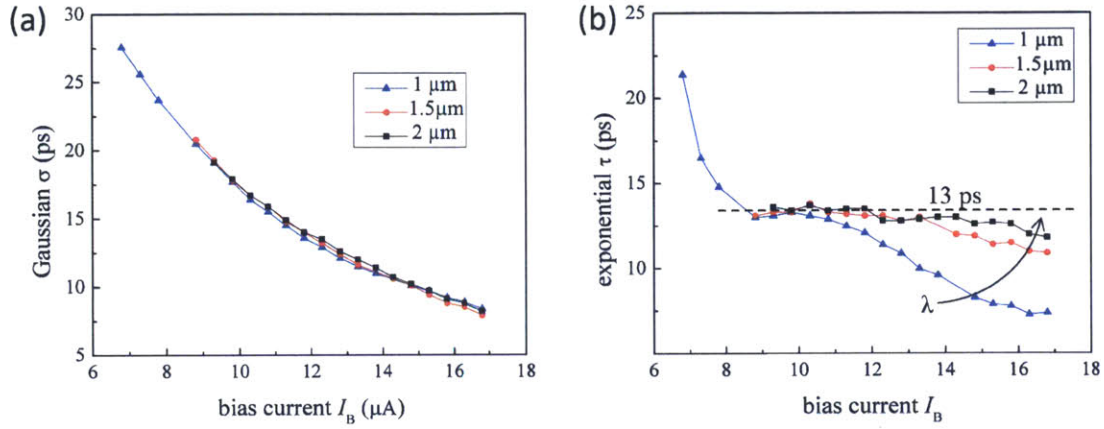


Figure 4-9: Fitting parameters  $\sigma$  (a) and  $\tau$  (b) as a function of bias current and wavelength for an SNSPD based on 100-nm-wide nanowires.

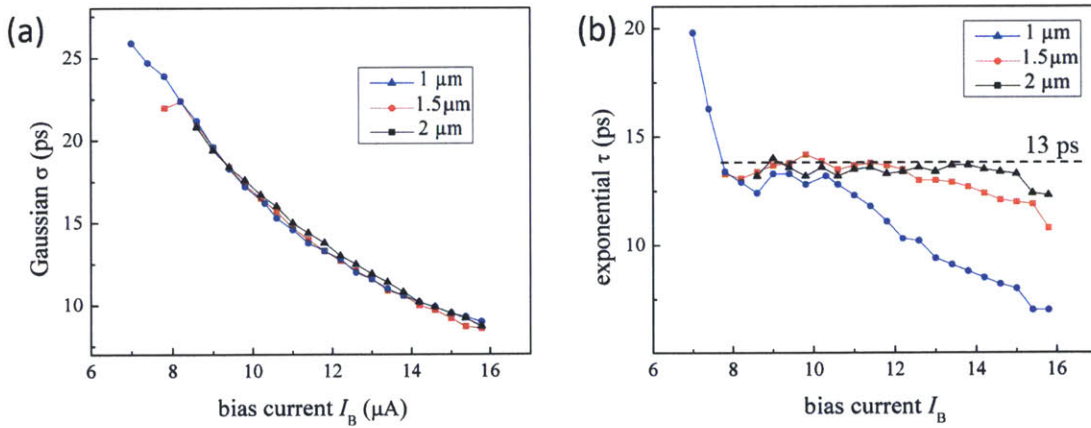


Figure 4-10: Fitting parameters  $\sigma$  (a) and  $\tau$  (b) as a function of bias current and wavelength for an SNSPD based on 85-nm-wide nanowires.

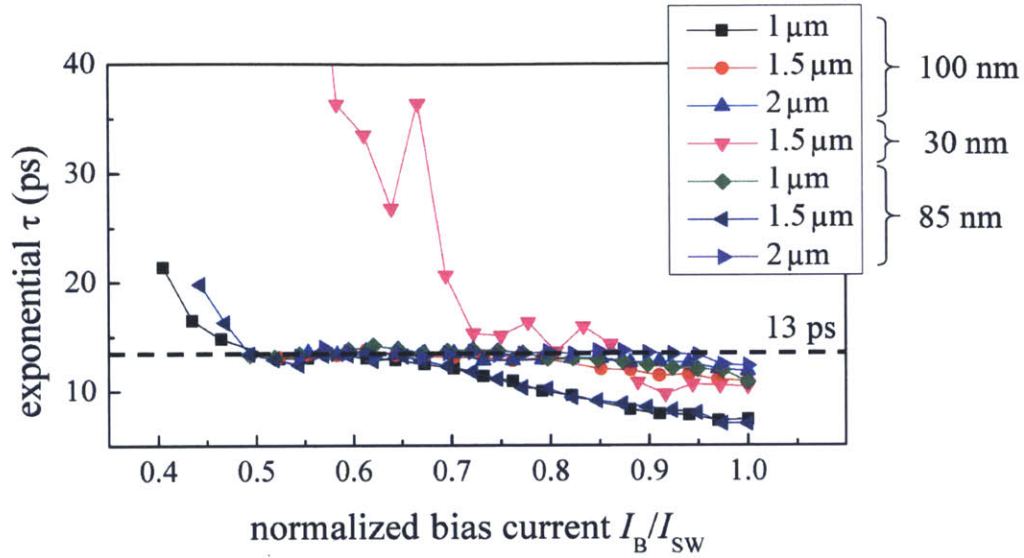


Figure 4-11: Exponential fitting parameter  $\tau$  for SNSPDs based on 30-, 85- and 100-nm-wide nanowires.  $\tau$  is shown at different wavelengths as a function of normalized bias current  $I_B/I_{SW}$ , where  $I_{SW}$  is the switching current of the corresponding SNSPD.

small compared to high bias currents, suggesting that the initial hotspot plays a larger relative role in creating the slab. Furthermore, the increasing  $\tau$  at higher photon energies is consistent with decreasing gap suppression time for increasing energies of the initial perturbation.  $\tau$  could also originate from vortex dynamics in the nanowire, outlined in chapter 5.



## Chapter 5

# Current flow and critical current in presence of a vortex in a superconducting strip

SNSPDs are based on thin superconducting strips which are two-dimensional superconductors. The transition from the superconducting state to the normal state is associated with a vortex entering the superconducting strip.

This transition event has some implications for device performance: (1) it limits the critical current of the detector and hence the signal-to-noise ratio and timing jitter; and (2) it is possibly associated with the energy- and bias-current-dependence of the device detection efficiency [30, 31]. Therefore understanding vortex motion could be crucial in improving SNSPD performance.

In this chapter we present a simple method for calculating the current distribution around a vortex inside near superconductor boundaries and inside a superconducting strip. Furthermore, we will briefly discuss the energy barrier for vortex entry into a superconducting strip and the effective critical current of a superconducting wire as a function of geometrical and film parameters.

## 5.1 3D superconductor

Before considering superconducting strips, we will introduce basic concepts regarding flux penetration and vortices in a 3-dimensional superconductor.

### 5.1.1 Surface energy: type I vs type II superconductor

A bulk superconductor at temperatures well below  $T_C$  and zero external fields and currents is in the Meissner state. In this state no flux enters the superconductor except at the surface within a distance on the order of the magnetic penetration depth  $\lambda$ . When increasing the external magnetic field (starting from zero field), a type I superconductor will transition from the flux-free Meissner state to the normal state (all the external flux enters the superconductor) once the external field has surpassed the critical field  $H_C(T)$ , as illustrated in Figure 5-1(a). In a type II superconductor there is an intermediate state between the Meissner and the normal state: the mixed state (Figure 5-1(b)). In this state flux enters the superconductor within regions of diameter  $\approx 2 \cdot \xi$  (where  $\xi$  is the coherence length) at locations which are organized in a hexagonal crystal structure (Figure 5-2(b)). The localized region where the flux enters the superconductor is called a vortex. Each vortex carries a flux of  $\Phi_0$ .

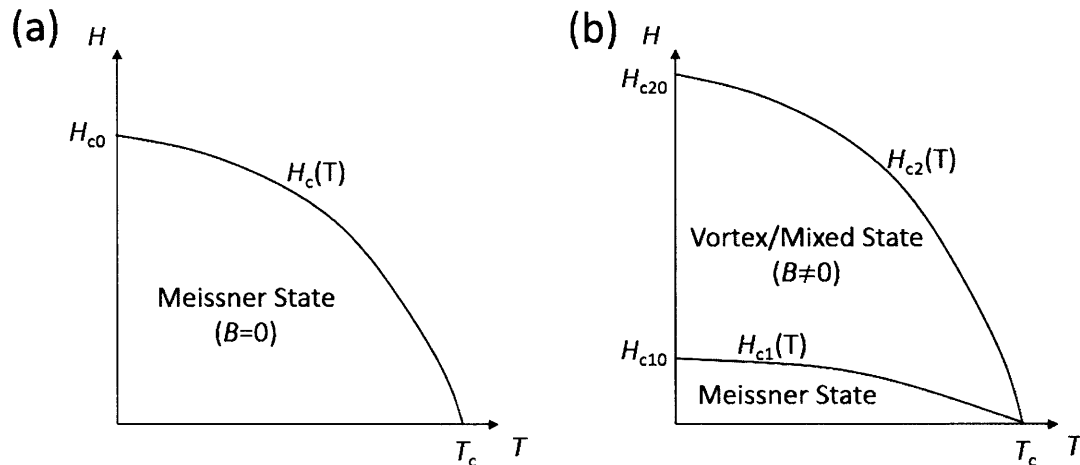


Figure 5-1: As in Ref. [45]. (a) Phase diagram of type I superconductor. (b) Phase diagram of type II superconductor.

In a constant magnetic field at constant temperature, (Gibb's) free energy is minimized:

$$dG = 0 \quad (5.1)$$

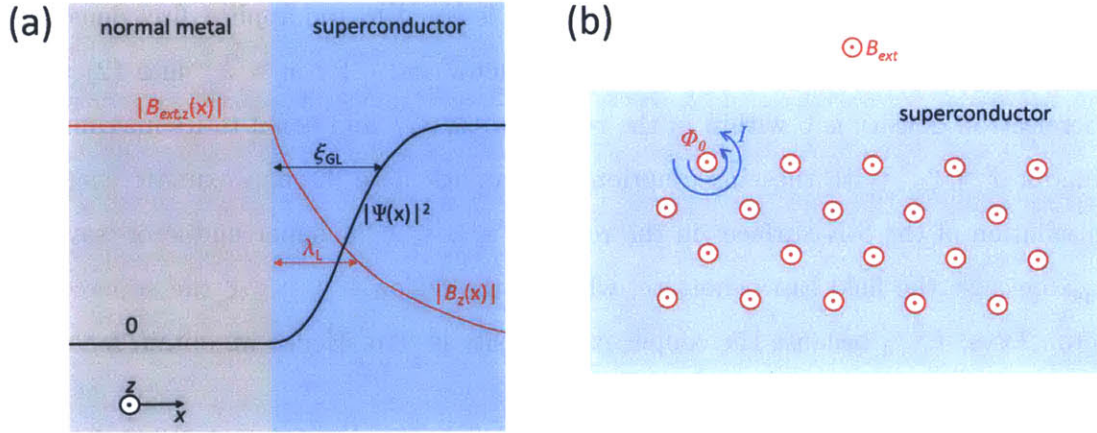


Figure 5-2: As in Ref. [46]. (a) Magnetic flux density and superelectron density at interface between superconductor and normal metal. (b) Vortices in mixed phase. Red circles illustrate the flux through the vortex core and blue arrows the circulating currents that shield the vortex from the rest of the superconductor.

We define the thermodynamic critical field  $B_{C,Th}(T)$  in terms of the condensation energy per volume

$$\frac{B_{C,Th}^2(T)}{2\mu_0} = \frac{E_{cond}}{V} = \frac{G_n(T) - G_{sc}(T)}{V} \quad (5.2)$$

where  $G_n(T)$  and  $G_{sc}(T)$  are the Gibbs free energies of the normal and superconducting state respectively. When external flux  $\alpha B_{ext}$  is applied, the superconductor will switch to the normal state once the energy  $E_{repel}$  needed to repel the magnetic flux exceeds the condensation energy. Whether a material is a type I or type II superconductor depends on the characteristic ratio  $\kappa = \frac{\lambda}{\xi}$ . An approximate dependence on  $\kappa$  can be obtained from the energy required to form a surface between superconducting and normal phases in the mixed state. Figure 5-2(a) shows a sketch of the

magnetic flux density (red curve) and superelectron density (black curve) at the interface between a superconducting (S) and normal metal (N). While the superelectron density gradually increases between 0 and its maximum value within a characteristic distance on the order of the coherence length  $\xi$ , the magnetic flux density penetrates the superconductor in a region of thickness  $\sim \lambda$ . Hence we can make the following approximations: (1) The magnetic flux density is equal to the applied flux density in the region  $0 \leq x \leq \lambda$  inside the superconductor and 0 for  $x > \lambda$ ; and (2) the superelectron density is 0 within in the region  $0 \leq x \leq \xi$  and equal to its maximum value for  $x > \xi$ . With these assumptions we can calculate the approximate energy contribution of the S-N surface: in the region  $0 \leq x \leq \lambda$  the superconductor 'saves'  $E_{\text{repel}}$  because the field can penetrate, while in the region  $0 \leq x \leq \xi$  the superconductor 'loses'  $E_{\text{cond}}$  because the cooper pair density is zero. Hence we obtain for the energy contribution of an S-N interface with area A:

$$\Delta E \approx \frac{A}{2\mu_0}(\xi B_{\text{C,Th}}^2 - \lambda B_{\text{ext}}^2) \quad (5.3)$$

For  $\lambda \gg \xi$  this energy contribution is negative and the coexistence of both phases is preferred (type II superconductor), whereas for a type I superconductor (here  $\lambda \ll \xi$ ) the contribution of the surface energy is positive and hence only one phase is preferred - more quantitative criteria for  $\kappa$  can be obtained with the Ginzburg-Landau equations.

### 5.1.2 Modified second London equation: fields and currents of bulk-superconductor vortices

We can calculate the spatial distribution of the magnetic flux density  $B(\vec{r})$  and current density  $J_s(\vec{r})$  of a high- $\kappa$ -superconductor ( $\lambda \gg \xi$ ) using the second London equation when assuming that the vortex has a well defined normal core of radius  $\xi$ . The assumptions in this section are (1) the bulk limit where all the dimensions of the superconductor are much larger than the magnetic penetration depth, and (2) a single vortex that is centered at  $r = 0$  within an infinitely large superconducting volume

(or deep within the superconductor so that no surface currents are present). In this picture, the second London equation

$$\nabla \times (\Lambda J_S) + B = 0 \quad (5.4)$$

is fulfilled for  $|\vec{r}| > \xi$ . However, a more accurate picture is that the cooper pair density only gradually drops to 0 at the center of the vortex (Figure 5-3), and 5.4 is fulfilled everywhere except at  $|\vec{r}| = 0$ . In order to account for the vortex core, we introduce the vorticity  $V(\vec{r})$  into 5.4 and obtain the modified second London equation

$$\nabla \times (\Lambda J_S) + B = V(\vec{r}) = \Phi_0 \delta(x) \delta(y) i_z \quad (5.5)$$

Here we assume that only one vortex is present. If the externally applied flux exceeds  $\sim \Phi_0$ , more than one vortex can enter the superconductor and we will have to adjust  $V(\vec{r})$  accordingly. By inserting the Maxwell equation

$$\nabla \times B = \mu_0 J_S \quad (5.6)$$

into 5.5 and using  $\nabla \cdot B = 0$  we obtain

$$\nabla^2 B - \frac{B}{\lambda^2} = \frac{-\Phi_0}{\lambda^2} \delta(x) \delta(y) i_z \quad (5.7)$$

This equation has the exact solution

$$B(r, \phi) = \frac{\Phi_0}{2\pi\lambda^2} K_0\left(\frac{r}{\lambda}\right) i_z = \frac{\Phi_0}{2\pi\lambda} \frac{e^{-r/\lambda}}{r} i_z \quad (5.8)$$

where  $K_0$  is the 0-th-order modified Bessel function of the second kind. For  $r \ll \lambda$  or at large distances from the core we can obtain the approximations

$$B(r \rightarrow \infty) \approx \frac{\Phi_0}{2\pi\lambda^2} \sqrt{\frac{\pi\lambda}{2r}} e^{-r/\lambda} i_z \quad (5.9)$$

$$B(\xi < r < \lambda) \approx \frac{\Phi_0}{2\pi\lambda} \frac{i_z}{r} \quad (5.10)$$

A schematic sketch of the cross section of the flux density and superelectron density around a vortex is shown in Figure 5-3.

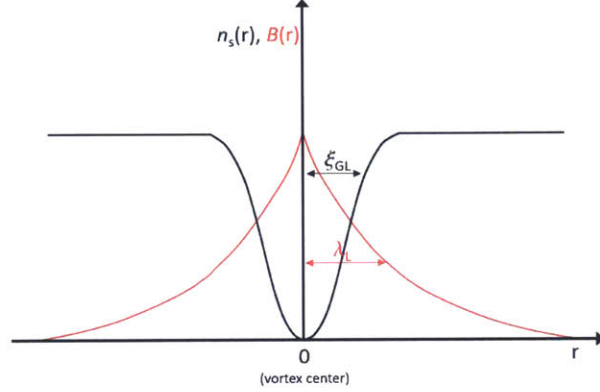


Figure 5-3: As in Ref. [46]. Spatial dependence of magnetic flux density and superelectron density around a bulk-superconductor vortex centered at  $r=0$ .

As expected, for large distances the magnetic flux density decreases exponentially within a characteristic distance on the order of the magnetic penetration depth. However, this behavior changes dramatically in thin films, as outlined in section 5.2.1. Now we can calculate the current density using 5.6. We obtain

$$J_S(r, \phi) = \frac{\Phi_0}{2\pi\mu_0\lambda^3} K_1\left(\frac{r}{\lambda}\right) i_\phi = \frac{\Phi_0}{2\pi\mu_0\lambda} \frac{\left(1 + \frac{r}{\lambda}\right) e^{-r/\lambda}}{r^2} i_\phi \quad (5.11)$$

with the limits

$$J_S(r \rightarrow \infty) \approx \frac{\Phi_0}{2\pi\mu_0\lambda^2} \frac{e^{-r/\lambda}}{r} i_\phi \quad (5.12)$$

$$J_S(\xi < r < \lambda) \approx \frac{\Phi_0}{2\pi\mu_0\lambda^2} \frac{i_\phi}{r^2} \quad (5.13)$$

A representation of the profile of  $J$  (5.11) is shown in Figure 5-5(a).

### 5.1.3 Vortex near bulk-superconductor boundary

We can use the results from the previous section to find solutions for  $J$  and  $B$  for a vortex near the boundary of a superconductor, as shown in Figure 5-4. The boundary condition for the vortex current is:

$$i_x \cdot J_S(x = 0) = 0 \quad (5.14)$$

, i.e. no current flow perpendicular to the boundary. We can use the image method to find a solution that fulfills this boundary condition.

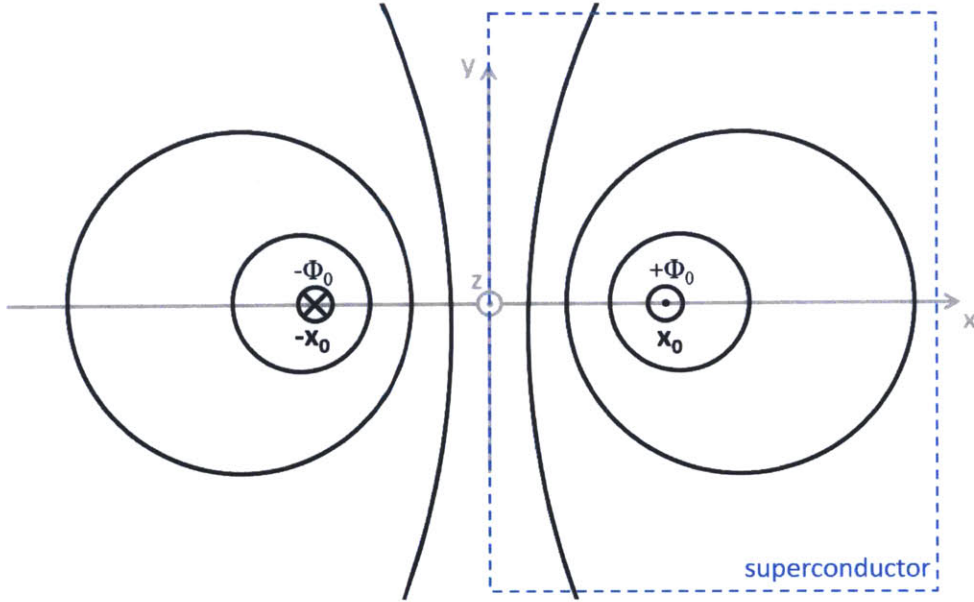


Figure 5-4: As in Ref. [45]. Schematic representation of field lines for the current density or magnetic vector potential obtained using the image vortex method to solve for the fields and currents around a vortex close to the boundary of a superconductor. The solution is only valid for  $x > 0$ .

Using the Cartesian form of 5.11

$$J_S^y(x - x_0, y) = \frac{\Phi_0}{2\pi\mu_0\lambda} \frac{\left(1 + \frac{\sqrt{(x-x_0)^2 + y^2}}{\lambda}\right) e^{-\sqrt{(x-x_0)^2 + y^2}/\lambda}}{((x-x_0)^2 + y^2)^{3/2}} (-yi_x + (x-x_0)i_y) \quad (5.15)$$

We can calculate the solution as

$$J_S(x \geq 0, y) = J'_S(x - x_0, y) - J'_S(x + x_0, y) \quad (5.16)$$

The profile of the current distribution 5.15 is shown in Figure 5-5(a), while current density distribution 5.16 is shown in Figure 5-5(b).

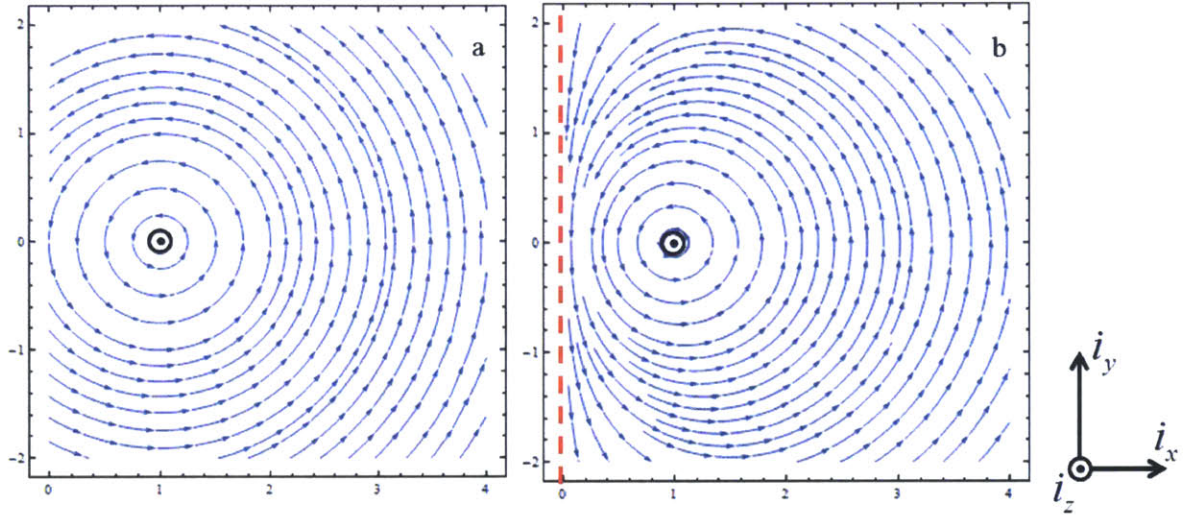


Figure 5-5: Vector fields representing the distribution and direction of the current density around a vortex centered at  $x = 1$  (a.u.) placed deep within a bulk superconductor (a) and close to the boundary ( $x = 0$  interface) of a bulk superconductor (b).

We can proceed accordingly for the magnetic field and magnetic flux density

$$B(x \geq 0, y) = B^\nu(x - x_0, y) - B^\nu(x + x_0, y) \quad (5.17)$$

## 5.2 2D superconductor

Having considered vortices introduced for 3-dimensional superconductors, we can now use a similar framework to describe vortices in thin superconducting strips and to calculate the corresponding current flow.

### 5.2.1 Vortex in thin superconducting strip

We use Pearl's solution of the modified second London Equation

$$\nabla \times (\Lambda J_S) + B = \Phi_0 \delta(z) \delta_2(r - r_0) \quad (5.18)$$

to calculate the vortex current density in a thin (thickness  $d \ll \lambda$ ) long (length  $l \gg \lambda$ ) narrow (width  $w \ll \frac{\lambda^2}{d}$ ) superconducting strip around a single vortex located at  $r_0$ . Any solution for the vortex current has to satisfy the boundary conditions, namely vanishing current perpendicular to the strip boundaries. Similar to the vortex near the boundary of a superconductor, outlined in section 5.1.3, we will use the image method to construct a solution for the surface current density  $K_S$  [47]. Pearl's approximate solution [48] for the surface current density

$$J_S = K_S \delta(z) \quad (5.19)$$

only differs from the exact solution by less than 10% in magnitude. The approximate solution

$$K_S(r, \phi) = \frac{\Phi_0}{\mu_0 \pi} \frac{i_\phi}{r(2\lambda_\perp + r)} \quad (5.20)$$

with the effective sheet penetration depth

$$\lambda_\perp = \frac{\lambda^2}{d} \quad (5.21)$$

, where  $d$  is the film thickness. This distribution has two limits:

$$K_S(r \gg \lambda_\perp, \phi) \approx \frac{\Phi_0}{\mu_0 \pi} \frac{i_\phi}{r^2} \quad (5.22)$$

$$K_S(\xi < r \ll \lambda_\perp, \phi) \approx \frac{\Phi_0}{\mu_0 \pi 2\lambda_\perp} \frac{i_\phi}{r^2} \quad (5.23)$$

Due to the large effective penetration depth, vortex currents in 2D superconductors fall off more slowly ( $\sim r^{-2}$ ) than in the bulk limit ( $\sim e^{-r/\lambda}$ ). However, the influence of the penetration depth on the current distribution becomes negligible close

to the vortex core, where we obtain a similar spatial distribution ( $\sim r^{-1}$ ) in both 2D and bulk cases.

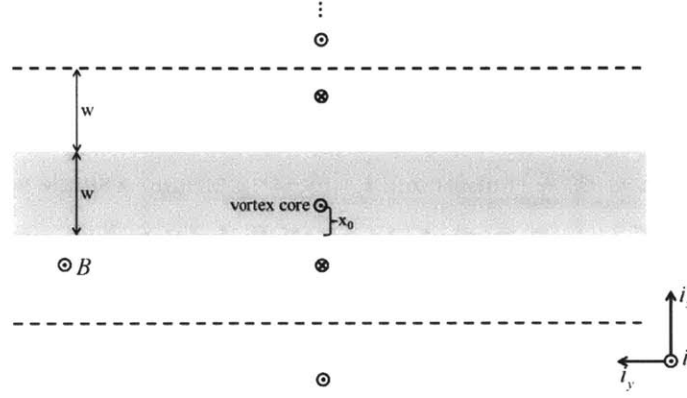


Figure 5-6: Vortex inside a narrow thin superconducting film (grey strip) centered at a distance  $x_0$  from the lower edge.

Figure 5-6 shows the geometry for which we will calculate the current distribution. The vortex is a distance  $x_0$  away from the lower edge of the strip. Here boundary conditions

$$\begin{aligned}
 K_S(|\vec{r}| \rightarrow \infty) &= 0 \\
 K_S(x = 0) &= 0 \\
 K_S(x = w) &= 0
 \end{aligned}
 \tag{5.24}$$

need to be satisfied at both edges. As a result a series of image charges are needed, unlike in the case where only one boundary is present. Using the method of images (see Figure 5-6) we obtain

$$\begin{aligned}
 K_S^{strip}(\vec{r}) &= K_S(\vec{r} - \vec{r}_0) - K_S(\vec{r} + \vec{r}_0) + \sum_{n=1}^{\infty} K_S(\vec{r} - (i_x 2wn + \vec{r}_0)) - \\
 &K_S(\vec{r} - (i_x 2wn - \vec{r}_0)) + K_S(\vec{r} - (-i_x 2wn + \vec{r}_0)) - K_S(\vec{r} - (-i_x 2wn - \vec{r}_0))
 \end{aligned}
 \tag{5.25}$$

Since the narrow strip geometry breaks the cylindrical symmetry of the problem, it is more convenient to proceed in Cartesian coordinates. From 5.20 we obtain

$$K_S(x - x_0, y) = \frac{\Phi_0}{\mu_0 \pi} \frac{-y i_x + (x - x_0) i_y}{((x - x_0)^2 + y^2) \left( 2\lambda_{\perp} + \sqrt{(x - x_0)^2 + y^2} \right)} \quad (5.26)$$

By using 5.26 in 5.25 and summing up 80 terms, we obtain the current distribution shown in Figure 5-7 and Figure 5-8(a).

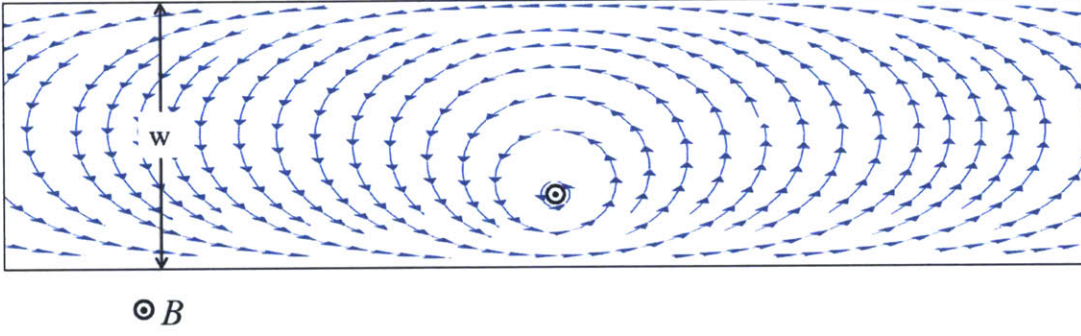


Figure 5-7: Vector field representing the surface current solution using 5.25 for the geometry shown in Figure 5-6.

It is evident from Figures 5-7 and 5-8(a) that our solution satisfies 5.24. Bulaevskii et al. [30] chose a different method than Orlando and Pearl to solve 5.18. Using the Green's function from [30]

$$G(\vec{r}) = \frac{\Phi_0 (1 - \kappa^2)}{2\pi\Lambda} \ln \left( \frac{\cosh\left(\frac{\pi y}{w}\right) - \cos\left(\frac{\pi(x+x_0)}{w}\right)}{\cosh\left(\frac{\pi y}{w}\right) - \cos\left(\frac{\pi(x-x_0)}{w}\right)} \right) \quad (5.27)$$

we calculate the surface current density  $K_S = \nabla \times (G(\vec{r}) i_z)$  and obtain

$$i_x \cdot K_S = \frac{\Phi_0 (1 - \kappa^2)}{2\Lambda w} \left( \frac{\sinh\left(\frac{\pi y}{w}\right)}{\cosh\left(\frac{\pi y}{w}\right) - \cosh\left(\frac{\pi(x+x_0)}{w}\right)} - \frac{\sinh\left(\frac{\pi y}{w}\right)}{\cosh\left(\frac{\pi y}{w}\right) - \cosh\left(\frac{\pi(x-x_0)}{w}\right)} \right) \quad (5.28)$$

$$i_y \cdot K_S = \frac{-\Phi_0(1 - \kappa^2)}{2\Lambda w} \left( \frac{\sin\left(\frac{\pi(x+x_0)}{w}\right)}{\cosh\left(\frac{\pi y}{w}\right) - \cosh\left(\frac{\pi(x+x_0)}{w}\right)} - \frac{\sin\left(\frac{\pi(x-x_0)}{w}\right)}{\cosh\left(\frac{\pi y}{w}\right) - \cosh\left(\frac{\pi(x-x_0)}{w}\right)} \right) \quad (5.29)$$

The current density according to Kogan's approach (plotted in Figure 5-8(b)) yields approximately the same distribution as Orlando's result 5.25.

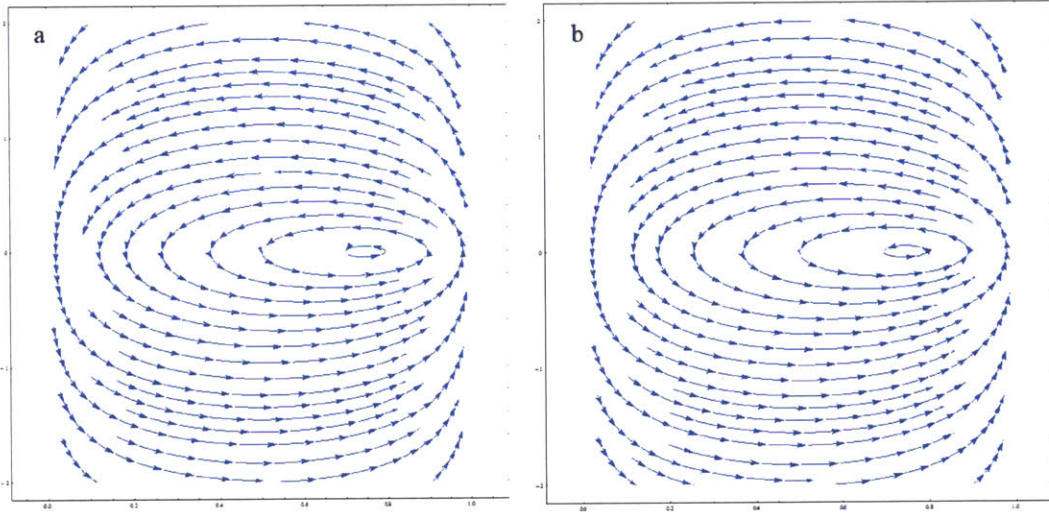


Figure 5-8: (a) Surface current density vector field for a narrow-strip vortex calculated with the image method. (b) Surface current density vector field for a narrow-strip vortex calculated from Kogan's function.

## 5.2.2 Photon-assisted vortex tunneling and possible implications for photodetection delay

Following Kogan [31] and Engel [32], the normalized potential energy of a vortex in a current-carrying superconducting strip is:

$$U(I, x) \propto \ln\left(\frac{2w}{\pi\xi} \sin\left(\frac{\pi}{w}x\right)\right) - \frac{I_B}{I_{C,v}} \frac{2}{e\xi}x \quad (5.30)$$

, where  $I_{C,v}$  is the critical current of the strip - note that  $\xi(T)$  results in a

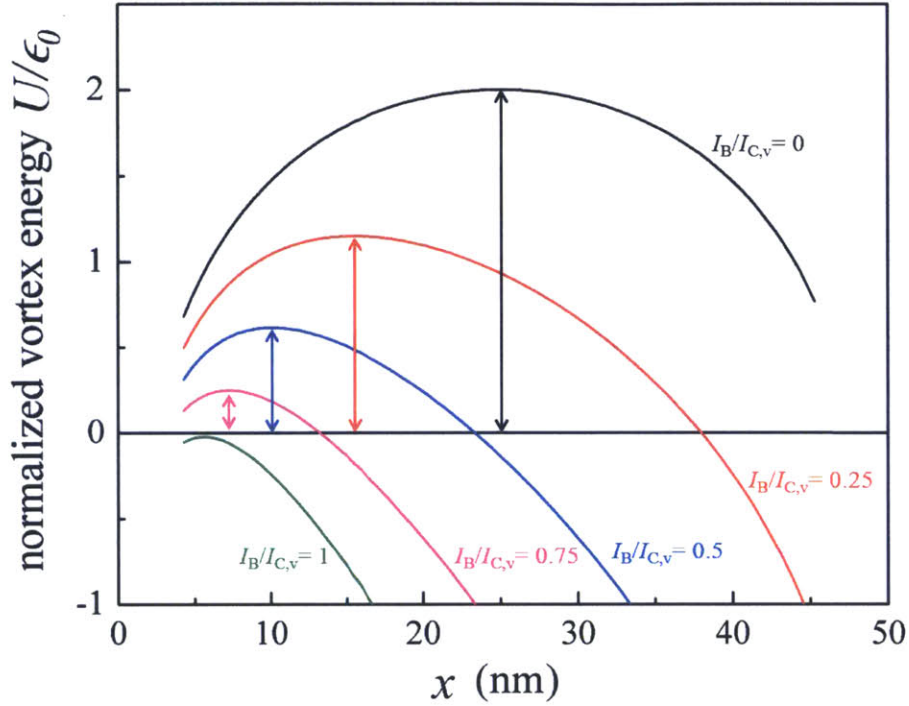


Figure 5-9: Potential energy of a vortex in a 50-nm-wide superconducting strip as described in Refs. [31, 32]. The energy, normalized by a scaling factor  $\epsilon_0$  [30], is shown for different bias currents. The arrows denote the height of the energy barrier for a vortex crossing.

temperature-dependence of  $U$ . Figure 5-9 shows the plotted potential energy along the strip at different bias currents. When biased at  $I_B < I_{C,v}$ , a voltage can be measured along the strip if a vortex overcomes a potential barrier of height  $U_{\max}(I, T)$  (see arrows in Fig. 5-9). Increasing bias currents and local temperatures, e.g. due to photon absorption, can (1) result in a reduced barrier height, making vortex tunneling (or vortex crossing due to thermal activation) more likely, or (2) increase the current density locally so that  $J_B > J_{C,v}$ , at which point the energy barrier vanishes (green curve in 5-9), resulting in a full transition of the wire to the normal state. In case (1) the photon count rate depends on bias current, while in case (2) the photon count rate should show a low dependence on bias current, which is qualitatively consistent with the bias-current-dependence of SNSPD photon count rates (e.g. see Fig. 1-9).

The characteristic relaxation time of the quasiparticle sea at the absorption site of

the photon is believed to be on the order of  $\tau_{qp} \sim 10ps$  [32, 24], i.e. the quasiparticle sea and therefore the local temperature relaxes at a rate  $exp(-t/\tau_{qp})$ . In the picture of vortex-assisted detection, the time-dependent temperature modulation would result in a corresponding time-dependence of the barrier height  $U_{max}$ . Higher photon energies would mean lower  $U_{max}(t = 0)$  therefore higher rate of counts at shorter  $t$ , resulting in a smaller IRF tail and smaller IRF asymmetry. In this picture, a higher bias current would have an effect similar to higher photon energies, which is qualitatively consistent with the experimental data in Fig. 4-11.

# Chapter 6

## Summary and outlook

### 6.1 Timing performance of ultranarrow SNAPs

We studied the instrument response function of 2-, 3-, and 4-SNAPs based on 30-nm-wide NbN nanowires. The measurements yielded the following results:

(1) When biased close to the switching current ( $I_{SW}$ ), the SNAP IRFs were symmetric and the sub-35-ps timing jitter comparable to SNSPDs. As the bias current was lowered, the IRFs shifted to longer time delays and became more broad and asymmetric. In avalanche regime, the increase in width and asymmetry of the IRF was significant at  $I_B = I_{AV}$ , indicating that there is a tradeoff between timing jitter (higher close to  $I_{AV}$ ) and dark count rate (lower close to  $I_{AV}$ ) when operating SNAPs.

(2) For  $I_B < I_{AV}$  we observed a sudden decrease in IRF width and asymmetry, indicating that low-bias SNAPs could be used in applications that require low-jitter multi-photon gates.

(3) We were able to reproduce the bias-current-dependence of the IRF time shift using a one-dimensional electrothermal model. However, at very low bias currents and for larger nanowire widths (see SNSPD section), the 1D model was not sufficient. Furthermore, our models could not explain the IRF asymmetry; the larger asymmetry may be caused by an increase in the time required by the current redistributed from the initiating section to suppress the superconducting gap in the secondary sections.

(4) Although the absolute values of the MLD and  $t_P$  were defined with respect to

different moments in time ( $t_{FPD}$  for the MLD and  $t_\xi$  for the  $t_P$ ), the current dependencies of the values of the MLD and  $t_P$  were similar across a broad  $I_B$  range, indicating that - when neglecting the effect of jitter - for ultranarrow nanowires the time difference  $t_{FPD}-t_\xi$  does not vary with bias current. This could mean that for narrow nanowires at high bias currents (i.e. for a saturated efficiency), the formation of the resistive slab is instantaneous, and that in this regime the initial photodetection process (e.g. hotspot generation) is current-independent ( $t_\xi-t_{HSN} = const.$  in saturation regime).

## 6.2 Timing performance of SNSPDs

We studied the behavior of the instrument response function as a function of width, bias current and wavelength, to our knowledge the first systematic study of this kind. The key findings were:

- (1) The one-dimensional electrothermal model did not sufficiently reproduce the photodetection delay (MLD) for nanowires wider than 50 nm at low bias currents.
- (2) The jitter of SNSPDs did not have a significant dependence on nanowire width or wavelength, and was mainly limited by the signal-to-noise ratio.
- (3) The asymmetric tail of the IRF increased with increasing wavelength.

A more accurate model is needed to understand the initial phases of photodetection. Considering the dependence of the MLD and asymmetry on the nanowire geometry, bias current and photon energy, a two-dimensional electrothermal model, incorporating gap suppression time or vortex motion in the initial stages of photodetection, appears to be a good candidate.

- (4) We could fit the IRFs with an exponentially-modified Gaussian with the fitting parameters  $\sigma$  and  $\tau$ . These parameters showed a distinct current-dependent behavior, possibly due to their origin from different physical processes during photodetection. At low bias currents and photon energies  $\tau$  reached a plateau of  $\sim 13$  ps.

### 6.3 Vortex-assisted photon counts

We showed a simple model for calculating the current flow in presence of a vortex in a superconducting strip. Furthermore, we discussed the bias-current- and photon-energy-dependence of energy barriers for vortex entry into superconducting nanowires. The results presented here could help understand the observed IRFs, and to improve our current models of photodetection in SNSPDs.



# Bibliography

- [1] Danna Rosenberg, Charles G. Peterson, Jim W. Harrington, Patrick R. Rice, N. Dallman, K. T. Tyagi, K. P. McCabe, Sae Woo Nam, B. Baek, R. H. Hadfield, Richard J. Hughes, and Jane E. Nordholt. Practical long-distance quantum key distribution system using decoy levels . *New J. Phys.*, 11(045009), 2009.
- [2] Alan Aspuru-Guzik and Philip Walther. Photonic quantum simulators. *Nat Phys*, 8(4):285–291, 04 2012.
- [3] Jeremy L. O’Brien, Akira Furusawa, and Jelena Vuckovic. Photonic quantum technologies. *Nature Photonics*, 3(12):687–695, 2009.
- [4] J M Amini, H Uys, J H Wesenberg, S Seidelin, J Britton, J J Bollinger, D Leibfried, C Ospelkaus, A P VanDevender, and D J Wineland. Toward scalable ion traps for quantum information processing. *New Journal of Physics*, 12(3):033031, 2010.
- [5] M. E. Grein, M. Willis, A. Kerman, E. Dauler, B. Romkey, D. Rosenberg, J. Yoon, R. Molnar, B. S. Robinson, D. Murphy, and D. M. Boroson. A fiber-coupled photon-counting optical receiver based on nbn superconducting nanowires for the lunar laser communication demonstration. *CLEO:2014, OSA Technical Digest*, page SM4J.5.
- [6] M.D. Shaw, J.A. Stern, K. Birnbaum, M. Srinivasan, M. Cheng, K. Quirk, A. Biswas, F. Marsili, V. B. Verma, R. P. Mirin, S. W. Nam, and W. H. Farr. Tungsten silicide superconducting nanowire arrays for the lunar laser octl terminal. *CLEO:2013 Technical Digest*, page QM4L.7.

- [7] Thorlabs photodiode power sensors (c-series). [http://www.thorlabs.com/newgrouppage9.cfm?objectgroup\\_id=3328](http://www.thorlabs.com/newgrouppage9.cfm?objectgroup_id=3328), 2015.
- [8] Robert Hadfield. Single-photon detectors for optical quantum information applications. *Nature Photonics*, 3:696–705, 2009.
- [9] Hamamatsu photomultiplier tubes. <http://www.hamamatsu.com/us/en/product/category/3100/3001/index.html>, 2015.
- [10] Adriana E. Lita, Aaron J. Miller, and Sae Woo Nam. Counting near-infrared single-photons with 95 *Optics Express*, 6(5):3032–3040, 2008.
- [11] Alberto Tosi, Niccolo Calandri, Mirko Sanzaro, and Fabio Acerbi. Low-noise, low-jitter, high detection efficiency ingaas/inp single-photon avalanche diode. *IEEE Journal of Selected Topics in Quantum Electronics*, 20(6):3803406, 2014.
- [12] G. N. Gol’tsman, O. Okunev, G. Chulkova, A. Lipatov, A. Semenov, K. Smirnov, B. Voronov, A. Dzardanov, C. Williams, and Roman Sobolewski. Picosecond superconducting single-photon optical detector. *Applied Physics Letters*, 79(6):705–707, 2001.
- [13] Thomas Gerrits, Brice Calkins, Nathan Tomlin, Adriana E. Lita, Alan Migdall, Richard Mirin, and Sae Woo Nam. Extending single-photon optimized superconducting transition edge sensors beyond the single-photon counting regime. *Optics Express*, 20(21):23798–23810, 2012.
- [14] Eric A. Dauler, Andrew J. Kerman, Bryan S. Robinson, Joel K. Yang, Boris Voronov, Gregory Gol’tsman, Scott A. Hamilton, and Karl K. Berggren. Photon-number-resolution with sub-30-ps timing using multi-element superconducting nanowire single photon detectors. *Journal of Modern Optics*, 56(2 & 3):364–373, January 2009.
- [15] Eric A. Dauler, Bryan S. Robinson, Andrew J. Kerman, Vikas Anant, Richard J. Barron, Karl K. Berggren, David O. Caplan, John J. Carney, Scott A. Hamilton,

- Kristine M. Rosfjord, Mark L. Stevens, and Joel K. Yang. 1.25 gbit/s photon-counting optical communications using a two-element superconducting nanowire single photon detector. *Proc. of SPIE Advanced Photon Counting Techniques, Wolfgang Becker*, 637212:3032–3040, 2006.
- [16] Catherine Lee, Zheshen Zhang, Gregory R. Steinbrecher, Hongchao Zhou, Jacob Mower, Tian Zhong, Ligong Wang, Xiaolong Hu, Robert D. Horansky, Varun B. Verma, Adriana E. Lita, Richard P. Mirin, Francesco Marsili, Matthew D. Shaw, Sae Woo Nam, Gregory W. Wornell, Franco N. C. Wong, Jeffrey H. Shapiro, and Dirk Englund. Entanglement-based quantum communication secured by nonlocal dispersion cancellation. *Physical Review A*, 90:062331, 2014.
- [17] A. Giudice, M. Ghioni, R. Biasi, F. Zappa, S. Cova, P. Maccagnani, and A. Gulinatti. High-rate photon counting and picosecond timing with silicon-spad based compact detector modules. *Journal of Modern Optics*, 54(2-3):225–237, 2007.
- [18] F. Marsili, V. B. Verma, J. A. Stern, S. Harrington, A. E. Lita, T. Gerrits, I. Vayshenker, B. Baek, M. D. Shaw, R. P. Mirin, and S. W. Nam. Detecting Single Infrared Photons with 93% System Efficiency. *arXiv:1209.5774*, September 2012.
- [19] Shigehito Miki, Taro Yamashita, Hirotaka Terai, and Zhen Wang. High performance fiber-coupled nbtin superconducting nanowire single photon detectors with gifford-mcmahon cryocooler. *Optics Express*, 21(8):10208–10214, 2013.
- [20] D. Rosenberg, A. J. Kerman, R. J. Molnar, and E. A. Dauler. High-speed and high-efficiency superconducting nanowire single photon detector array. *Optics Express*, 21(2):1440–1447, 2013.
- [21] F. Marsili, V. B. Verma, J. Stern, S. Harrington, A. Lita, T. Gerrits, I. Vayshenker, B. Baek, M. Shaw, R. Mirin, and S. W. Nam. Detecting single infrared photons with 93% system efficiency. *Nat Photon*, 7(3):210–214, 03 2013.

- [22] W. Pernice, C. Schuck, O. Minaeva, M. Li, G. N. Gol'tsman, A. V. Sergienko, and H. X. Tang. High Speed and High Efficiency Travelling Wave Single-Photon Detectors Embedded in Nanophotonic Circuits. *Nature Communications*, 3:1325, 2012.
- [23] Francesco Marsili, Francesco Bellei, Faraz Najafi, Andrew E. Dane, Eric A. Dauler, Richard J. Molnar, and Karl K. Berggren. Efficient Single Photon Detection from 500 nm to 5  $\mu$ m Wavelength. *Nano Letters*, 12(9):4799–4804, 2012.
- [24] A. Semenov, G. Gol'tsman, and A. Korneev. Quantum detection by current carrying superconducting film. *Physica C*, 351:349–356, 2001.
- [25] Francesco Marsili, Faraz Najafi, Eric Dauler, Francesco Bellei, Xiaolong Hu, Maria Csete, Richard J. Molnar, and Karl K. Berggren. Single-Photon Detectors Based on Ultranarrow Superconducting Nanowires. *Nano Letters*, 11(5):2048–2053, 2011.
- [26] William E. Keicher Joel K. W. Yang Karl K. Berggren Andrew J. Kerman, Eric A. Dauler. Kinetic-inductance-limited reset time of superconducting nanowire photon counters. *Applied Physics Letters*, 88:111116, 2006.
- [27] Joel K. W. Yang, Andrew J. Kerman, Eric A. Dauler, Vikas Anant, Kristine M. Rosfjord, and Karl K. Berggren. Modeling the electrical and thermal response of superconducting nanowire single-photon detectors. *IEEE Transactions on Applied Superconductivity*, 17:581–585, 2007.
- [28] Francesco Marsili, Faraz Najafi, Eric Dauler, Hasan Korre, Vikas Anant, Kristen Sunter, and Karl K. Berggren. Cavity-Integrated Ultra-Narrow Superconducting Nanowire Single-Photon Detector Based on a Thick Niobium Nitride Film. In *CLEO: QELS-Fundamental Science*, page QTu3E.3. Optical Society of America, 2012.
- [29] Andrew J. Kerman, Eric A. Dauler, Joel K. W. Yang, Kristine M. Rosfjord, Vikas Anant, Karl K. Berggren, Gregory N. Gol'tsman, and Boris M. Voronov.

- Constriction-limited detection efficiency of superconducting nanowire single-photon detectors. *Applied Physics Letters*, 90(10):101110, 2007.
- [30] L. N. Bulaevskii, M. J. Graf, C. D. Batista, and V. G. Kogan. Vortex-induced dissipation in narrow current-biased thin-film superconducting strips. *Physical Review B*, 83:144526, 2011.
- [31] L. N. Bulaevskii, M. J. Graf, and V. G. Kogan. Vortex-assisted photon counts and their magnetic field dependence in single-photon superconducting detectors. *Physical Review B*, 85:014505, 2012.
- [32] A. Engel and A. Schilling. Numerical analysis of detection-mechanism models of superconducting nanowire single-photon detector. *Journal of Applied Physics*, 114:214501, 2013.
- [33] J. J. Renema, R. Gaudio, Q. Wang, Z. Zhou, A. Gaggero, F. Mattioli, R. Leoni, D. Sahin, M. J. A. de Dood, A. Fiore, and M. P. van Exter. Experimental test of theories of the detection mechanism in a nanowire superconducting single photon detector. *Physical Review Letters*, 112:117604, 2014.
- [34] M. Ejrnaes, R. Cristiano, O. Quaranta, S. Pagano, A. Gaggero, F. Mattioli, R. Leoni, B. Voronov, and G. Gol'tsman. A cascade switching superconducting single photon detector. *Applied Physics Letters*, 91:262509, 2007.
- [35] F. Najafi, F. Marsili, E. Dauler, R.J. Molnar, and K.K. Berggren. Timing performance of 30-nm-wide superconducting nanowire avalanche photodetectors. *Applied Physics Letters*, 100(15):152602–152602–4, 2012.
- [36] F. Marsili, F. Najafi, E. Dauler, R. J. Molnar, and K. K. Berggren. Afterpulsing and instability in superconducting nanowire avalanche photodetectors. *Applied Physics Letters*, 100(11):–, 2012.
- [37] J. Zhang, W. Slysz, A. Pearlman, A. Verevkin, Roman Sobolewski, O. Okunev, G. Chulkova, and G. N. Gol'tsman. Time delay of resistive-state formation in

- superconducting stripes excited by single optical photons. *Physical Review B*, 67:132508, 2003.
- [38] Michael G. Tanner, Vadim Makarov, and Robert H. Hadfield. Optimised quantum hacking of superconducting nanowire single-photon detectors. *Optics Express*, 22(6):6734-6748, 2014.
- [39] Faraz Najafi. *Characterization of Superconducting Nanowire Single-Photon Detectors*. Diploma Thesis, TU Munich, 2010.
- [40] Francesco Marsili, Faraz Najafi, Charles Herder, and Karl K. Berggren. Electrothermal simulation of superconducting nanowire avalanche photodetectors. *Applied Physics Letters*, 98:093507, 2011.
- [41] J. A. O'Connor, M. G. Tanner, C. M. Natarajan, G. S. Buller, R. J. Warburton, S. Miki, Z. Wang, S. W. Nam, and R. H. Hadfield. Spatial dependence of output pulse delay in a niobium nitride nanowire superconducting single-photon detector. *Applied Physics Letters*, 98:201116, 2011.
- [42] Martin J. Stevens, Robert H. Hadfield, Thomas Gerrits, Tracy S. Clement, Richard P. Mirin, and Sae Woo Nam. Infrared wavelength-dependent optical characterization of nbn nanowire superconducting single-photon detectors. *Journal of Modern Optics*, 56:358-363, 2009.
- [43] M. Ejrnaes, A. Casaburi, R. Cristiano, O. Quaranta, S. Marchetti, N. Martucciello, S. Pagano, A. Gaggero, F. Mattioli, R. Leoni, P. Cavalier, and J. C. Villegier. Timing jitter of cascade switch superconducting nanowire single photon detectors. *Applied Physics Letters*, 95:132503, 2009.
- [44] Michael Tinkham. *Introduction to Superconductivity*. Dover Publications, Inc., 2004.
- [45] T. Orlando and K. Delin. *Foundations of Applied Superconductivity*. Addison Wesley Publishing Company, 1991.

- [46] R. Gross. *Solid State Physics, Lecture Notes*. Oldenbourg Verlag, tpb. 2012.
- [47] T. Orlando. Part i. upper critical fields and spin states in a-15 superconductors : Part ii. vortices in two-dimensional superconductors. *Ph.D. Thesis*, 1981.
- [48] J. Pearl. Vortex theory of superconductive memories. *Ph.D. Thesis*, OSTI ID 4562822, 1965.